Periodic Motions and Stability Analysis of a Non-linear Rotating Beam Subjected to Torsional Excitation

by Yuhui Qu, Bachelor of Engineering

A Thesis Submitted in Partial
Fulfillment of the Requirements
for the Degree of
Master of Science
in the field of Mechanical Engineering

Advisory Committee:

Fengxia Wang, Chair
Keqin Gu
Soondo Kweon

Graduate School
Southern Illinois University Edwardsville
August, 2014

ABSTRACT

PERIODIC MOTIONS AND STABILITY ANALYSIS OF A NON-LINEAR ROTATING BEAM SUBJECTED TO TORSIONAL EXCITATION

by

YUHUI QU

Chairperson: Professor Fengxia Wang

The periodic motions and stability of a nonlinear rotating beam subjected to a torsional excitation is investigated in this thesis. Both quadratic and cubic geometric stiffening nonlinearities are retained in the equation of motion, and the reduced model is obtained via the Galerkin method. Saddle-node bifurcations and Hopf bifurcations of the Period-1 motions of the model were obtained via the high order harmonic balance method. The period-2 and period-4 solutions, which are emanated from the period-1 and period-2 motions, respectively, are obtained by the combined implementation of the harmonic balance method, Floquet theory, and Discrete Fourier Transform (DFT). Stabilities are detected by Floquet theory. Stable and unstable periodic motions are illustrated from numerical and analytical solutions. The analytical periodic solutions and their stabilities are verified through numerical simulation.

ACKNOWLEDGEMENTS

I would like to express my heartfelt gratitude to my graduate advisor, Dr. Fengxia Wang, without whom none of the work presented in this thesis would have been accomplished. I want to thank her for her humility, patience and guidance throughout this research. I am also grateful for her financial support for my study. It was a great pleasure working for her.

I want to especially thank all the other members of my thesis advisory committee, Dr. Keqin Gu and Dr. Soondo Kweon who have been always supportive and ready to help whenever necessary.

I am grateful to Professor Dr. Ryan Fried in Department of Civil Engineering for his financial support and help. Also I wish to express my appreciation to all the faculty and staff at Southern Illinois University for all the cooperative efforts during my study.

I would also like to acknowledge the support from the members in our lab, who have created a peaceful and joyful environment for me to work in. I feel so honored to have them in graduate studies. I also would like to express my appreciation to all my friends for their help on my research and daily life.

Sincerely, I thank my parents for their love, encouragement, enthusiasm and support.

TABLE OF CONTENTS

LIST OF FIGURES

LIST OF FIGURES

LIST OF TABLES

CHAPTER I

INTRODUCTION

Literature Survey

The vibration problem of rotating beams has been extensively studied by researchers in both aerospace and mechanical engineering due to its important applications such as helicopter, turbine blades, and appendages of spinning satellites.

The study of vibrations of rotating beams can be traced back to the work of Schilhansil in 1958. In his research, the partial differential equation was obtained by assuming steady state revolution and the geometric stiffening was approximated by the centrifugal force. Similarly, Hurty and Rubistein(1964) accounted for the geometric stiffening effect in the studying of the dynamics of a beam vibration by considering only the axial component of the centrifugal force. The linear partial differential equation for flexural vibration based on linearization of nonlinear equations of motion was attained by Anderson (1975). Kane, Ryan, and Banerjee (1987) derived the strain energy of a rotating beam, in which the nonlinear strain-displacement relation is implicitly included, though it is not apparent due to the choice of independent variables. Simo and Vu-Quoc (1987) studied numerical stability issues of a rotating beam, and pointed out the importance of considering nonlinear geometric stiffening effects in the stability analysis. Sharf (1995) studied the nonlinear expression of the internal force based on nonlinear kinematics. He then derived the quadratic and cubic geometric nonlinear stiffness matrices of Euler-Bernoulli beams (1996-1999). To solve this problem, various analytical and numerical methods such as Rayleigh-Ritz method, Galerkin's method (1998), and finite element method (1997-1999) have

been employed and compared to obtain successive results.

The dynamical behavior of the linear model of a rotating blade, in which the geometric stiffening effect is approximated by an effective load, is governed by a set of Mathieu–Hill equations. Turhan and Bulut (2005) studied the stability of the linear model of a rotating beam with one single bending mode through a monodromy matrix method and the so called generalized Bolotin method (2003).

While the linear stability analysis of a rotating beam can provide precise stable and unstable regions in terms of system parameters, these stability results only give a rough outline for vibration testing due to the neglect of nonlinear effect in the model. Once the system parameters go beyond the linear stability region, the effects of nonlinearities will emerge, and the linear model will no longer be satisfied. Therefore the nonlinear vibrations of a rotating shaft have drawn large amount of research attention since the 1970s. Carnegie et.al (1970) found that large amplitudes of the second harmonic occur at frequencies less than the natural frequency of a uniform untwisted rotating cantilever blade. This shows that nonlinearities play an important role as the speed of rotation become large. In the work of Friedmann et.al (1989), a finite-element model was built from Hamilton's principle and the geometrically nonlinear behavior was considered based upon the moderate deflection theory. Turhan et.al (2008) obtained the one degree and two degree nonlinear model of a rotating beam based on the Galerkin method and analyzed the amplitude frequency response via the perturbation method. Similarly, Zhang et.al (2012) studied a thin-walled rotating beam via the multiple time scale perturbation method. The average equations are obtained for the 1:1 internal resonance and primary resonance cases, and then the numerical simulations are applied to the average equations to illustrate the existence of periodic motions and chaotic motions. Shahgholi et.al

(2011) studied the effect of the eccentricity and external damping of an in-extensional spinning shaft, and the amplitude responses of periodic solutions are obtained by the harmonic balance method. Wang and Luo (2012-2013) studied stabilities of the period-1 motions of a rotating blade with the "geometric stiffening" nonlinearities via the generalized harmonic balance method (2012). Both Saddle-node bifurcations and Hopf bifurcations are observed in the period-1 motion of a rotating blade.

Thesis Objectives

From available nonlinear rotating shaft literature, we can see that most researchers focus on either modeling, or seeking steady state solutions, or both.

Two modeling approaches are primarily employed: one is Hamilton's principle with the Galerkin method and the other is the finite element method. The perturbation method or the harmonic balance method is typically applied to obtain the stability and bifurcations of steady state solutions. Whether our study subject is a turbine blade or an appendage of spinning satellites, one important goal of the study is to better understand structure failure, especially failure caused by fatigue.

Considering that the vibration frequency plays a significant role in stress intensity, crack propagation rate, and the final number of fatigue cycles to fracture (1995), besides the amplitudes, the steady state solution's frequency variations are also very important. The steady state solutions' frequency won't always follow the external excitation frequency. For example, as system parameters change, period-1 solution may lose stability and a stable period-2

solution may occur. In real experiments, the presence of the stable period-2 motion will lead to a sudden change of the vibration frequency, and hence will affect the structure failure factors.

In this thesis, we focus on the seeking of the period-2 and period-4 motions which are generated through Hopf bifurcations via the higher order harmonic balance method. Higher order harmonic balance methods have attracted lots of interests from nonlinear dynamics community over the past three decades. The basic theory of harmonic balance method is to transform the nonlinear dynamics problem into a set of nonlinear algebraic equations by truncated Fourier series (1979, 1996). To obtain an accurate enough solution for complicated nonlinear problems especially for the accurate prediction of bifurcations, one usually resorts to high order harmonic balance method. Various approaches for the implementation of the harmonic balance method have been proposed, including harmonic balance combined with Newton Raphson method (1981), incremental harmonic balance (1981-1983), time/frequency domain alternative harmonic balance (1989), and the generalized hamornic balance method—a combination of temporal variation with traditional harmonic balance method (2012-2013). In electrical circuit and control area, the harmonic balance method together with the Hopf bifurcation theory has also been widely used to predict the periodic solutions (1979, 1993, and 2002).

To improve the computation efficiency and successfully capture the period-2 solution generated by the Hopf bifurcations of period-1 solutions, in this work, higher order harmonic balance method, Floquet theory, and Discrete Fourier Transform are combined to be applied to the fluctuation rotating beam. Unlike the time/frequency domain alternative harmonic balance method(1989), in which iterations of Discrete Fourier Transform are performed in order to obtain one steady state solution, in our work to reduce the computation cost, the DFT is only

employed at Hopf bifurcation point to predict the initial guess of the new generated period-2 solutions.

Thesis Layout

This thesis consists of six chapters. Chapter I will give a literature survey on the investigations of the vibration of rotating beams. The thesis objectives and layout will also be presented. In Chapter II, the mechanical model of a nonlinear rotating blade subjected to a torsional excitation will be presented. The kinetic energy and strain energy of the system will be analyzed and the equations of motion will be derived. In Chapter III, the analytical solutions and their stability of periodic motions will be obtained via the high order harmonic balance method. The Saddle-node bifurcations and the Hopf bifurcations of the periodic solutions will be identified. Based on Hopf bifurcation theory, period-2 solutions, which are emanated from the period-1 solutions at the Hopf bifurcation points, will be captured. The stability of the generated period-2 and period-4 solutions will be evaluated via the Multiplier frequency method. The analytical predictions and the stability of the period-1, period-2, and period-4 motions will be verified by the numerical simulations in Chapter IV. Chapter V will summarize the results accomplished in this thesis.

CHAPTER II

EQUATION OF MOTION

In this chapter, the mechanical model of a nonlinear rotating beam subjected of torsional excitation will be illustrated. The kinetic energy and strain energy of the rotating beam will be analyzed and finally the equation of motion will be derived.

Mechanical Model

Consider an arbitrary flexible beam as shown in Fig.1. A moving frame "$oxyz$" is attached to the rigid non-deformed body which is rotating and the fixed frame "$OXYZ$" is the inertial frame. Coordinate x and y locates the position of an arbitrary point p of the non-deformed beam in the moving frame, and the axial and transverse deformation displacements of the arbitrary point p are u_p and v_p. Similarly, u and v represent the axial and transverse deformation displacements of a point on the neutral axis corresponding to the point p in the moving frame, hence we have,

$$u_p = u - y\sin\alpha, \tag{2.1}$$

$$v_p = v - y(1-\cos\alpha). \tag{2.2}$$

From the Euler-Bernoulli theory, the location and deformation vectors $\mathbf{t}_p^r$ and $\mathbf{u}_p^r$ of point p are

$$\mathbf{t}_p^r = [x, y, 0]^{\mathrm{T}}, \tag{2.3}$$

$$\mathbf{u}_p^r = [u - y\sin\alpha, v - y(1-\cos\alpha), 0]^{\mathrm{T}}. \tag{2.4}$$

With the assumption $v' < 1$ and $u' \ll 1$, $\alpha = v' + o(v'^2)$ where $v' = \partial v / \partial x$ is the first order approximation of $\alpha = \arctan[v'/(1+u')]$.

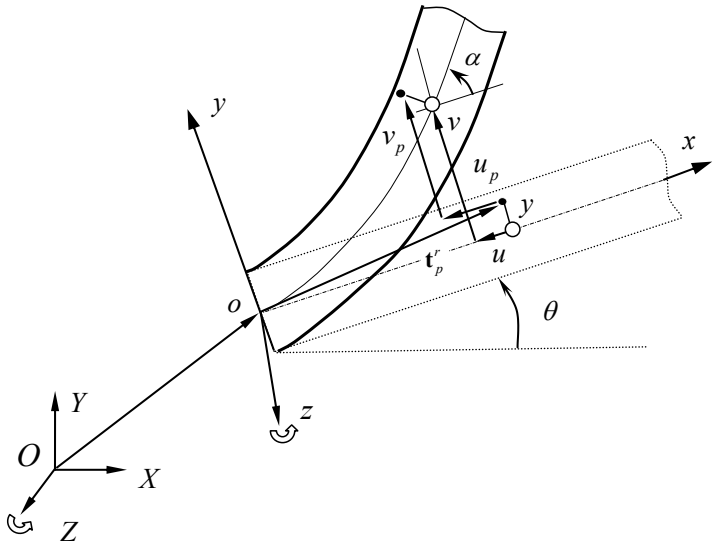

Fig. 1 Deformed configuration of a flexible body.

Kinetic Energy

The kinetic energy of an arbitrary small mass in the beam can be represented in either inertial frame or the moving frame. The location vector $\mathbf{t}_p^r$ does not change with time, i.e., . Thus, the velocity vector at point p is $\dot{\mathbf{t}}_p^r = \mathbf{0}$

$$\mathbf{v} = \dot{\mathbf{u}}_p^r + \boldsymbol{\omega} \times (\mathbf{t}_p^r + \mathbf{u}_p^r) \tag{2.5}$$

where $\dot{\mathbf{u}}_p^r = d\mathbf{u}_p^r / dt$ and the rotation velocity is

$$\boldsymbol{\omega} = [0, 0, \dot{\theta}]^{\mathrm{T}} \tag{2.6}$$

where the $\dot{\theta} = \frac{\partial \theta}{\partial t}$.

Thus, the total kinetic energy of a planar slender beam is

$$T = \frac{1}{2}\int_V \rho \mathbf{v} \cdot \mathbf{v} dV. \tag{2.7}$$

Substitution of Eqs.(2.1) - (2.6) into Eq.(2.7) yields the total kinetic energy of a rotating beam, i.e.,

$$\begin{aligned} T = \frac{1}{2}\int_0^L \{\rho A[\dot{u}^2 + \dot{v}^2 + 2\dot{\theta}(\dot{v}(u+x) - \dot{u}v) + \dot{\theta}^2((u+x)^2 + v^2)] \\ + \rho J[\dot{v}'^2 + 2\dot{\theta}\dot{v}' + \dot{\theta}^2]\} dx \end{aligned} \tag{2.8}$$

where $\dot{u} = \frac{\partial u}{\partial t}$, $\dot{v} = \frac{\partial v}{\partial t}$.

In Eq.(2.8), L is the total length of the beam, A is the cross section area of the beam, and J is the moment of inertia of cross section. Since the effect of rotary inertia is small in thin beam, the ρJ term in Eq.(2.8) will be dropped.

Strain Energy

For a two-dimensional Euler-Bernoulli beam, the shear strain is very small, which can be ignored. Neglecting the effect of shear deformation, the nonlinear normal strain can be expressed as

$$\varepsilon_x = \frac{\partial u_p}{\partial x} + \frac{1}{2}(\frac{\partial v_p}{\partial x})^2. \tag{2.9}$$

Substitution Eqs.(2.1) - (2.2) to Eq.(2.9), we can obtain

$$\varepsilon_x = \frac{\partial u}{\partial x} - y\alpha'\cos\alpha + \frac{1}{2}(\frac{\partial v}{\partial x} - y\alpha'\sin\alpha)^2. \quad (2.10)$$

The strain energy of a planar slender beam is

$$U = \frac{1}{2}\int_V (E\varepsilon_x^{\ 2} + G\varepsilon_{xy}^{\ 2})dV, \quad (2.11)$$

where E and G are Young's modulus and shear modulus, respectively. As mentioned above, for a two-dimensional Euler-Bernoulli beam, the shear strain can be ignores. Without the shear strain energy, substitution of Eq.(2.10) to Eq.(2.11), the strain energy of the two-dimensional Euler-Bernoulli beam is approximated as

$$U = \frac{1}{2}\int_0^L EA(u'^2 + u'v'^2 + \frac{1}{4}v'^4)dx + \frac{1}{2}\int_0^L EJ\,v''^2 dx \ . \quad (2.12)$$

Equation of Motion

Consider the transverse and longitudinal displacements to be expressed by the Galekin series,

$$u(x,t) = \sum_{j=1}^{n} \phi_{uj}(x) q_{uj}(t), \quad (2.13)$$

$$v(x,t) = \sum_{j=1}^{n} \phi_{vj}(x) q_{vj}(t), \quad (2.14)$$

where $\phi_{uj}(x)$ and $\phi_{vj}(x)$ are bending modes and longitudinal modes of a cantilever beam for the fixed-free boundaries as

$$\phi_{uj}(x) = \sin(\beta_{uj} x_1), \quad (2.15)$$

$$\phi_{vj}(x) = \cosh(\beta_{vj} x_1) - \cos(\beta_{vj} x_1) - \lambda_{vj}[\sinh(\beta_{vj} x_1) - \sin(\beta_{vj} x_1)], \quad (2.16)$$

where $x_1 = x/L$, and the parameters (β_{vj} , λ_{vj} , β_{uj}) are obtained from characteristic equations of a cantilever beam. These modes are based on the linear cantilever beam with the fixed-free boundary conditions, i.e.,

$$u(0,t) = 0 \tag{2.17}$$

$$u'(l,t) = 0 \tag{2.18}$$

$$v(0,t) = v'(0,\mathrm{t}) = 0 \tag{2.19}$$

$$v'''(l,t) = v'''(l,t) = 0 \tag{2.20}$$

Without loss of generality, one transverse mode and one longitudinal mode plus viscous damping are considered. For simplicity, we can consider a fluctuating rotation speed in the form of

$$\dot{\theta} = \bar{\psi}_0 + \bar{\psi}_1 \sin(\bar{\Omega}t). \tag{2.21}$$

Substitution of Eqs.(2.13) - (2.21) into the total energy equation and application of Hamilton's principle produces non-dimensional differential equation

$$\begin{bmatrix} \ddot{q}_1 \\ \ddot{q}_2 \end{bmatrix} + \mathbf{C}\begin{bmatrix} \dot{q}_1 \\ \dot{q}_2 \end{bmatrix} + \mathbf{K}\begin{bmatrix} q_1 \\ q_2 \end{bmatrix} + \mathbf{N}(q_1, q_2) = \mathbf{f}, \tag{2.22}$$

where damping and stiffness matrices are

$$\mathbf{C} = \begin{bmatrix} \delta_1 & 2\sigma(\psi_0 + \psi_1 \sin\Omega t) \\ -2\sigma(\psi_0 + \psi_1 \sin\Omega t) & \delta_2 \end{bmatrix}, \tag{2.23}$$

$$\mathbf{K} = \begin{bmatrix} \omega_1^2 - (\psi_0 + \psi_1 \sin\Omega t)^2 & \sigma\psi_1\Omega\cos\Omega t \\ \sigma\psi_1\Omega\cos\Omega t & \omega_2^2 - (\psi_0 + \psi_1 \sin\Omega t)^2 \end{bmatrix}. \tag{2.24}$$

and nonlinear term and force vectors are

$$\mathbf{N}(q_1, q_2) = \begin{bmatrix} \mu_1 q_1 q_2 + \mu_3 q_1^3 \\ \mu_2 q_1^2 \end{bmatrix}, \tag{2.25}$$

$$\mathbf{f} = \begin{bmatrix} (\psi_1 \Omega \cos \Omega t)\eta_v \\ (\psi_0 + \psi_1 \sin \Omega t)^2 \eta_u \end{bmatrix}. \tag{2.26}$$

The other terms in the equations above are

$$\omega_1 = \beta_{v1}^2 \sqrt{\frac{EJ}{\rho A L^4}}, \tag{2.27}$$

$$\omega_2 = \frac{\beta_{u1}^2}{\beta_{v1}^2} \sqrt{\frac{AL^2}{J}}, \tag{2.28}$$

$$\sigma = \int_0^1 \phi_{v1} \phi_{u1} dx_1, \tag{2.29}$$

$$\eta_v = -L \int_0^1 x_1 \phi_{v1} dx_1, \tag{2.30}$$

$$\eta_u = L \int_0^1 x_1 \phi_{u1} dx_1, \tag{2.31}$$

$$\mu_1 = \frac{AL^2}{\beta_{v1}^4 J} \int_0^1 (\phi_{v1}')^2 \phi_{u1}' dx_1, \tag{2.32}$$

$$\mu_2 = \frac{AL^2}{2\beta_{v1}^4 J} \int_0^1 (\phi_{v1}')^2 \phi_{u1}' dx_1, \tag{2.33}$$

$$\mu_3 = \frac{AL}{2\beta_{v1}^4 J} \int_0^1 (\phi_{v1}')^4 dx_1, \tag{2.34}$$

where dot denotes the derivative with respect to t. δ_1, δ_2 are the viscous damping coefficients. Stability analysis of the nonlinear equations with quadratic term kept in the axial direction equation and cubic term kept in the transverse direction equation will be studied.

Equation Section 3

CHAPTER III

PERIODIC SOLUTIONS

In this chapter, the analytical solutions and their stability of periodic motions will be obtained via the high order harmonic balance method. The Saddle-node bifurcations and the Hopf bifurcations of the periodic solutions will be identified. Based on Hopf bifurcation theory period-2 solutions, which are emanated from the period-1 solutions at the Hopf bifurcation points, will be captured. The stability of the generated period-2 and period-4 solutions will be evaluated via the Multiplier frequency method.

Disadvantage and Advantage of Other Methods

Among various version of higher order harmonic balance method, incremental harmonic balance and generalized harmonic balance are widely used to calculate parametric stability boundary for nonlinear systems.

As a combined application of variation, incremental harmonic balance steps from a known state of vibration to a neighboring state with an incremental change in one of the governing parameters of the system. Incremental harmonic balance can provide parametric stability boundary for linear system and the parametric stability region of a periodic solution for nonlinear systems. However, the incremental harmonic balance is computationally expensive.

The generalized harmonic balance method allows the Fourier series coefficients vary slowly with time. The stabilities and bifurcation types of periodic solutions can be evaluated through the eigenvalues of the time variant coefficients of every harmonic term. The generalized

harmonic balance method can efficiently trace the parametric stability boundary for both linear system and a periodic solution of a nonlinear system with good accuracy. From the convergence study of the generalized harmonic balance method, the stabilities and bifurcations are more sensitive to the number of harmonic terms finally retained in the analytical solution compared to the amplitudes of periodic solutions. The amplitude always converges much faster than the stability, which is determined by the eigenvalues of the temporal equations of each harmonic term's coefficient. For example, for the two degree of freedom strong nonlinear system described by Eq.(2.22), 8 harmonic terms will provide a fundamental resonance periodic solution with precision up to 1e-6. However, the periodic motion's stability obtained by the generalized harmonic balance method won't converge even with 24 harmonic terms when the solution is close to the bifurcation point.

Harmonic Balance Method Combined with Discrete Fourier Transform

To circumvent this disadvantage of the generalized harmonic balance method, reduce the number of harmonic terms, and yet with accurate estimation of both amplitude and stability, the synthetic implementation of the harmonic balance method, the Newton Raphson method, the Floquet theory, and the Discrete Fourier transform is employed in this thesis. Similar to the traditional harmonic balance method, the coefficients of each harmonic term are still assumed to be constant and the steady state solutions' stabilities and bifurcations are determined by the Floquet theory. As the system parameters change, last step's solution of each harmonic term's coefficient can be used as the initial guess of the current step's calculation in the Newton Raphson estimation. However at bifurcation points, a new branch of solution occurs and a

proper initial guess of the Fourier coefficients of the new solution is critical for the harmonic balance method to successfully trace down the new branch of periodic motion. For example, at the Hopf bifurcation point the period-1 solution lose stability at the same time the period-2 solution is generated. Capturing this new generated period-2 solution is not trivial, and an arbitrary initial guess of the Fourier coefficients typically won't converge to the stable period-2 solution. In order to obtain an accurate enough initial guess of the Fourier coefficients of the new generated solution, Discrete Fourier Transform (DFT) is employed to estimate the Fourier coefficients of the new solution. The implementation process is described as the following.

Analytical Periodic Solutions

The periodic solution of Eq.(2.22) can be written in Fourier series of the form,

$$\begin{bmatrix} q_1(t) \\ q_2(t) \end{bmatrix} \approx \mathbf{b}_0 + \sum_{i=1}^{\infty} \mathbf{a}_{i/m} \sin(\frac{i}{m}\Omega t) + \mathbf{b}_{i/m} \cos(\frac{i}{m}\Omega t), \tag{3.1}$$

where,

$$\begin{aligned} \mathbf{a}_{i/m} &= [a_{(i/m)1}, a_{(i/m)2}]^{\mathrm{T}}, \\ \mathbf{b}_{i/m} &= [b_{(i/m)1}, b_{(i/m)2}]^{\mathrm{T}}. \end{aligned} \tag{3.2}$$

In Eq.(3.1), m is a integer. For fundamental period-1 motion, m equals 1. For period-2 motion or period-4 motion, m equals 2 or 4, respectively.

Eqs.(3.3) - (3.4) define each harmonic term's amplitude and phase of the solutions of the bending and axial mode,

$$A_{i/m,1} = \sqrt{a_{i/m,1}^2 + b_{i/m,1}^2}, \ \phi_{i/m,1} = \arctan\frac{a_{i/m,1}}{b_{i/m,1}}, \tag{3.3}$$

$$A_{i/m,2} = \sqrt{a_{i/m,2}^2 + b_{i/m,2}^2},\ \phi_{i/m,2} = \arctan\frac{a_{i/m,2}}{b_{i/m,2}}. \tag{3.4}$$

Stability of Periodic Solutions

To obtain the stability of the periodic solutions, the Floquet multiplier is calculated. The multipliers are the functions of system parameters as presented in the work of Ajjarapu et.al (1992). When system parameters vary, some of the multipliers may cross the unit circle on the complex plane. The multiplier crossing the unit circle on the complex plane is called the critical multiplier. For a stable periodic motion, all multipliers are inside the unit circle, as the system parameter changes one multiplier may cross the unit circle and the stable periodic motion loses its stability.

There are three ways for a stable periodic solution to lose stability as showed in Fig.2, which associate with three types of critical multipliers.

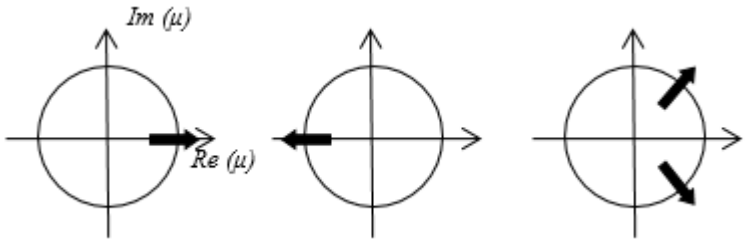

(a) (b) (c)

Fig.2 Three ways of losing stability.

A critical multiplier may go outside the unit circle along the positive real axis as showed in Fig.2 (a), which means turning points of the periodic orbit or a saddle node bifurcation occurs.

If the multiplier goes outside the unit circle along the negative real axis as showed in Fig.2 (b), period doubling or Hopf bifurcation occurs. If a pair of complex conjugate multipliers crosses the units circle with a non-zero imaginary part as showed in Fig.2 (c), then a secondary Hopf bifurcation or generalized Hopf bifurcation occurs.

The continuation calculation of periodic solution with parameter dependence is applied in the thesis. Once a periodic solution corresponding a set of specific system parameters $\Omega^*, \Psi_0^*,$ and Ψ_1^* is obtained, the Floquet theory is used to detect any bifurcations. Suppose one of the active parameters, Ω, is changed with an increment $\Delta\Omega$, the initial guess of the new periodic solution or the predictor will be estimated through different ways based on the bifurcation detection results:

(1) If the last step's periodic solution is not a bifurcation point, the predictor is given by the tangential continuation method, then applying the Gauss Newton method as a corrector to calculate the final solution;

(2) If the last step's solution is a saddle node or turning point bifurcation, the predictor is obtained by flipping the tangential guess about the radius of curvature at the turning point, and then obtain the final solution via the Gauss Newton calculation;

(3) If the last step's solution is a Hopf bifurcation point, first obtain the unstable period-1 solution as case (1). Obtain the initial condition of the unstable period-1 solution through harmonic balance reconstruction, time integral the original dynamic system with the initial condition, and achieve a steady state orbit.

The predictor of the newly generated stable period-2 solution can be estimated by applying DFT to the steady state orbit. Then the period-2 solution can be found by applying the Gauss

Newton method. During Fourier transformation, aliasing and leakage can corrupt the DFT values.

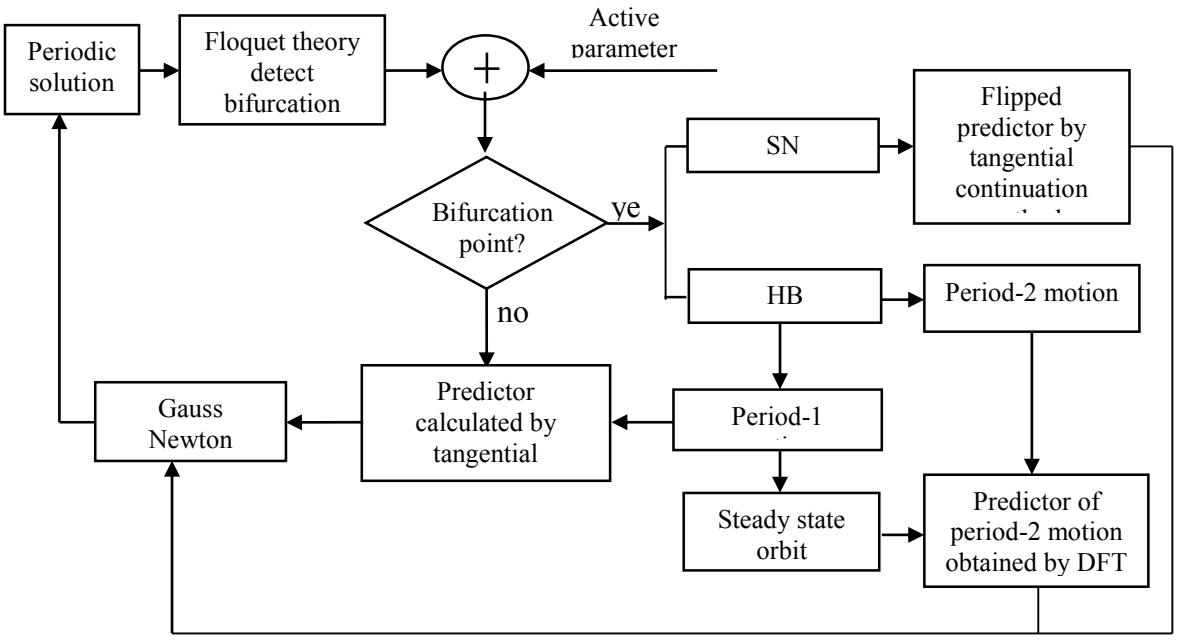

Fig. 3 The high order harmonic balance, Floquet theory, and Discrete Fourier Transform implementation flow chart.

To eliminate aliasing and leakage, the sampling data is synchronized and also choose the sampling frequency is chosen to be larger than twice of the frequency of the period-2 solution. The predicted Fourier coefficients of the period-2 solutions, which are solved by DFT is given in Eq. (3.5), where vector $\mathbf{q}_r = [q_{1r}(t), q_{2r}(t)]^{\mathrm{T}}$, $J = \sqrt{-1}$, $\Im$ denotes the imaginary part of a complex number and $\Re$ denotes the real part.

The implement flow chart of the described procedure is given in Fig.3.

$$\mathbf{b}_0 = \frac{1}{N}\sum_{r=0}^{N-1}\mathbf{f}(\mathbf{q}_r),$$
$$\mathbf{b}_{k1} = -\frac{2}{N}\Im\left\{\sum_{r=0}^{N-1}\mathbf{f}(\mathbf{q}_r)e^{J(-\frac{2\pi kr}{N})}\right\}, \tag{3.5}$$
$$\mathbf{a}_{k1} = \frac{2}{N}\Re\left\{\sum_{r=0}^{N-1}\mathbf{f}(\mathbf{q}_r)e^{J(-\frac{2\pi kr}{N})}\right\},$$

Bifurcation of Periodic Solutions

The above procedure will be applied to analyze system(2.22), and the following beam properties are considered

$$E = 69\text{GMa},\ \rho = 2712\text{kg/m}^3,\ A = 0.0002\text{m}^2,\ J = 2.5\times10^{-9}\text{m}^4,\ L = 1.5\text{m} \tag{3.6}$$

The Fourier series expression from Eq.(3.1). In nonlinear system need infinite terms to obtain the exact solution of the periodic motion. However, it is impossible for practice. Thus, the truncated Fourier series solutions will be used to give an approximate solution that can be close to the exact solution.

To achieve an accurate prediction of periodic motions, the number of harmonic terms retained in the analytical solution is determined based on the steady state solutions' convergence analysis. The steady state solution's convergence behavior is monitored by the following average norm,

$$\|q_i\| = \frac{1}{T}\int_0^T q_i(t)dt, \quad i = 1,2. \tag{3.7}$$

A solution with N_h harmonic terms is considered to be accurate if the average norms converge to the targeted precision. Based on the convergence criteria in Eq.(3.7), in this thesis, 32

harmonic terms of the Fourier series expansion are retained to obtain an accurate period-1 solutions and 64 harmonic terms are used to calculate period-2 solutions.

The analytical solutions of each harmonic term's amplitude and phase for period-1 motions, period-2 motions, and period-4 motions are presented in Fig.4 to Fig.12, as the external excitation frequency near the natural frequency of the first bending mode.

The constant term amplitude $A_{0,1}$ of the bending mode versus excitation frequency is plotted in Fig.4. From Fig.4, we can see that the periodic solutions clearly have a lower branch and an upper branch. From now on, we will separate all the periodic solutions into lower branch periodic solutions and upper branch periodic solutions. The upper branch is a loop which starts at Saddle-node SN_5^1 and ends at SN_8^1.

Fig.5 presents the constant coefficient $A_{0,2}$ versus frequency of the axial mode for the lower branch and Fig.6 presents for the upper branch.

The solid and dashed lines are curves representing the stable and unstable periodic solutions, respectively. On the diagrams, the acronyms SN and HB represent the Saddle-node and Hopf bifurcations respectively. Each SN and HB acronym has superscript and subscript, the superscripts 1, 2, and 4 represent bifurcations occurred on period-1, period-2, and period-4 motions, respectively. The subscript represents the order of the bifurcations. The notation "P-1", "P-2" and "P-4" represent period-1, period-2 and period-4 motions, respectively.

For period-1 motion, the Hopf bifurcation points are noted by stars. For period-2 motion, the Hopf bifurcation points are noted by triangles. The dark solid and dark dashed curves represent the stable and unstable period-2 solutions, respectively. In terms of period-4 solution, which are emanated through the Hopf bifurcation points of period-2, 128 harmonic terms are

retained in the analytical solutions. Similarly, solid double dark line and dashed double dark line represent stable and unstable period-4 solutions, respectively. Hopf bifurcation also presents in the period-4 solution, which are denoted by diamonds. We expect that at these Hopf bifurcation points of the period-4 solution, a stable period-8 solution will be generated. To present a clearer figure, the period-8 solutions didn't show in this thesis.

In the Fig.7, the fractional harmonic terms' amplitudes are plotted and the corresponding Hopf bifurcations are labeled. Fig.7 (a) & (b) are the amplitudes of the 1/4 harmonic term, which only exist in the period-4 motion. Fig.7 (a) are the amplitudes of the period-4 solutions of the bending mode, while Fig.7 (b) are the amplitudes of the period-4 solutions of the axial mode. Fig.7 (c) & (d) are the amplitudes of the 1/2 harmonic terms, which exist in both period-2 and period-4 solutions, and Fig.7 (c) is for the bending mode and Fig.7 (d) is for the axial mode. Fig.7 (e) & (f) are the amplitudes of the 3/4 harmonic term, which only exist in the period-4 motion, again Fig.7 (e) corresponds to the bending mode and Fig.7 (f) corresponds to the axial mode.

In the Fig.8 (a), the lower branch of the first harmonic term's amplitudes of the bending mode is represented. Fig.8 (b), (c) and (d) are the partially zoom in of Fig.8 (a). Fig.9 (a) is the upper branch of the first harmonic terms' amplitudes of the bending mode, and Fig.9 (b), (c) and (d) are the partially zoom in of Fig.9 (a).

In the Fig.10 (a), the lower branch of the first harmonic term's amplitudes of the axial mode is represented. Fig.10 (b), (c) and (d) are the partially zoom in of Fig.10 (a). Fig.11 (a) is the upper branch of the first harmonic terms' amplitudes of the bending mode, and Fig.11 (b), (c) and (d) are the partially zoom in of Fig.11(a).

The bifurcation scenario is listed in detail in Tab. 1.

Branches	Solution	Bifurcation	Ω value	Bifurcation Description
Lower Branch	Period-1	SN_1^1	0.6865	Between these two SN points, 1 unstable period-1 solution coexists with 2 stable period-1 solutions. Fig.4 (b); Fig.5 (a).
		SN_2^1	0.6131	
		HB_1^1	0.6759	Between these two HB points, period-1 solution loses stability and a stable period-2 solution is generated. Fig.4 (a); Fig.5 (c); Fig.5 (d).
		HB_2^1	0.8640	
		SN_3^1	0.9641	Between these two SN points, 3 period-1 solutions coexist and the middle one is unstable. Fig.4 (a); Fig.5 (a).
		SN_4^1	0.9205	
		HB_3^1	0.9453	Between these two HB points, period-1 solution loses stability and a stable period-2 solution is generated. Fig.4 (c); Fig.5 (b).
		HB_4^1	1.0055	
	Period-2	HB_1^2	0.6860	Between these two HB points, period-2 solution loses stability and a stable period-4 solution is generated. Fig.4 (e); Fig.5 (e); Fig.5 (f).
		HB_2^2	0.8188	
	Period-4	HB_1^4	0.7392	Between these two HB points, period-4 solution loses stability. A stable period-8 solution is expected, which is not shown in the figure. Fig.4 (e); Fig.5 (e); Fig.5 (f).
		HB_2^4	0.7990	
Upper Branch	Period-1	SN_5^1	1.0701	Between these two SN points, 2 period-1 solution coexists and one is unstable. Fig.4 (a); Fig.5 (a).
		SN_8^1	0.6653	
		HB_5^1	0.9998	Between these two HB points, period-1 solution loses stability and a stable period-2 solution is generated. Fig.4 (d); Fig.5 (b).
		HB_6^1	0.9510	
		SN_6^1	0.9218	Between these two SN points, 3 period-1 solutions coexist and the middle one isunstable. Fig.4 (a); Fig.6 (a).
		SN_7^1	0.9639	
		HB_7^1	0.8601	Between these two HB points, period-1 solution loses stability and a stable period-2 solution is generated. Fig.4 (a); Fig.6 (c); Fig.6 (d).
		HB_8^1	0.6856	
	Period-2	HB_3^2	0.8051	Between these two HB points, period-2 solution loses stability and a stable period-4 solution is generated. Fig.4 (f); Fig.6 (e); Fig.6 (f).
		HB_4^2	0.6957	
	Period-4	HB_3^4	0.7287	Between these two HB points, period-4 solution loses stability. A stable period-8 solution is expected, which is not shown in the figure. Fig.4 (f); Fig.6 (e); Fig.6 (f).
		HB_4^4	0.7058	

Tab.1 Bifurcation scenario.

Figs.12 are the phase plots of the first harmonic term for the bending mode. Figs.12 (b) - (h) are the partially zoom in of Fig.12 (a). Figs.13 are the first harmonic term's phase plots for the axial mode, and Figs.13 (b) - (f) are the partially zoom in of Fig.12 (a).

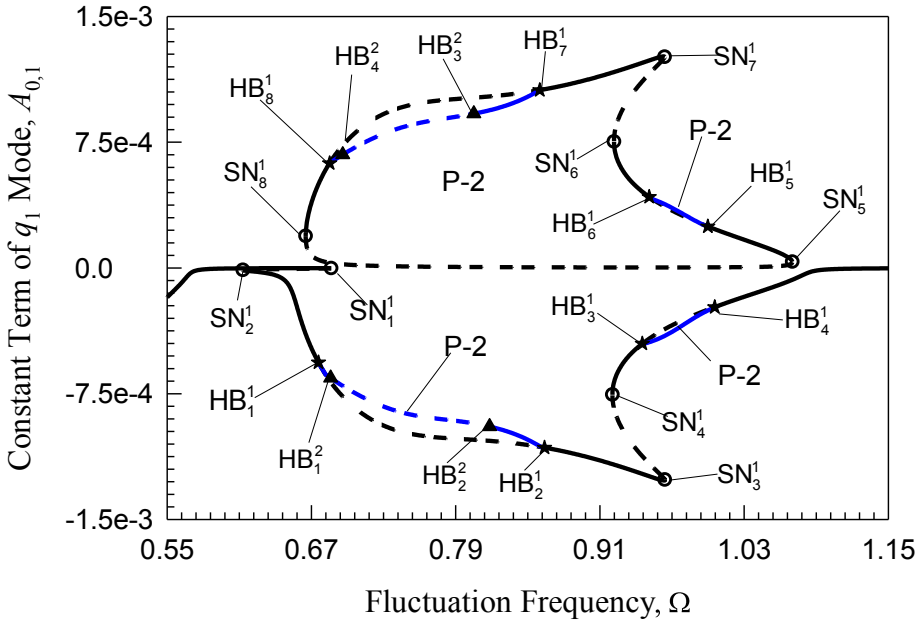

(a)

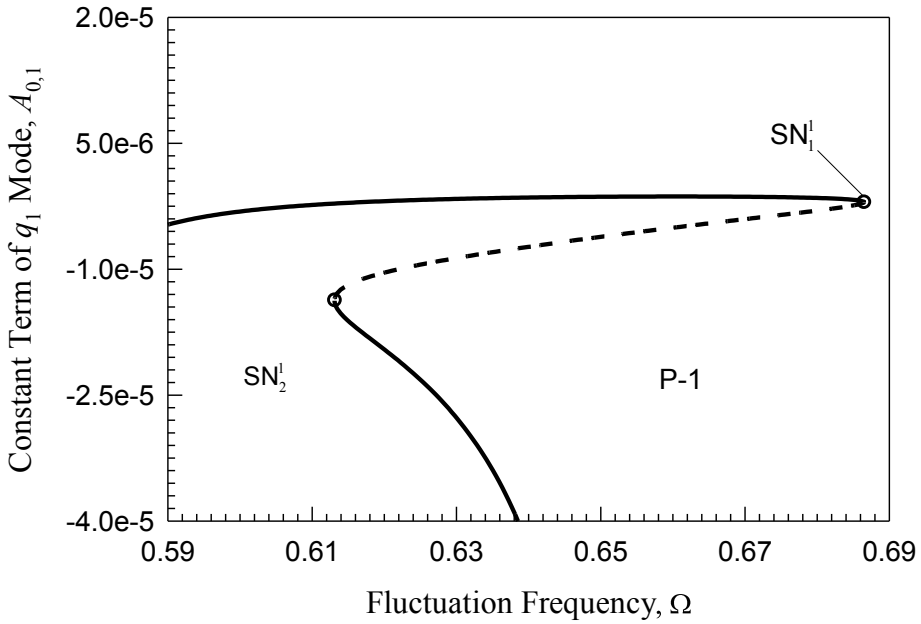

(b)

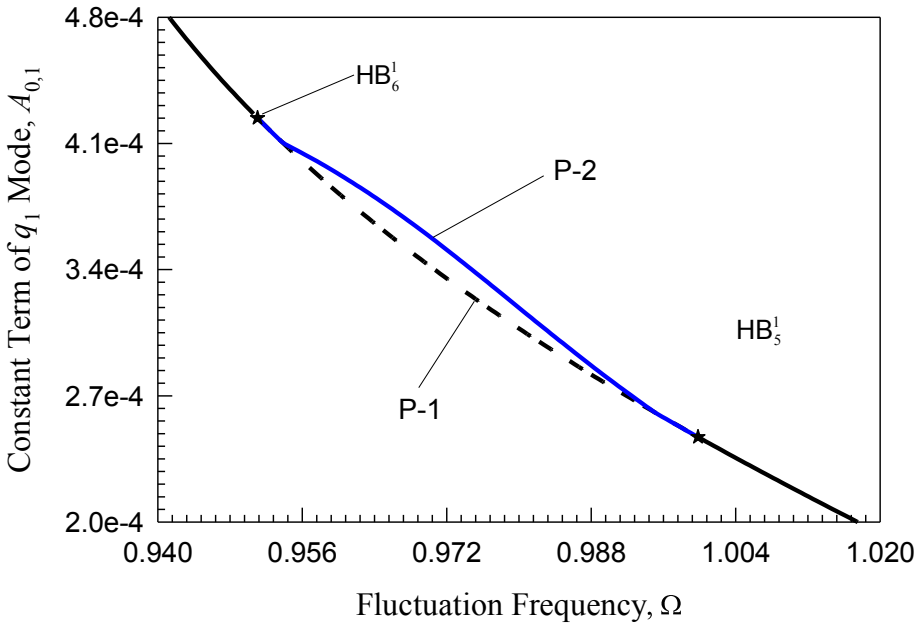

(c)

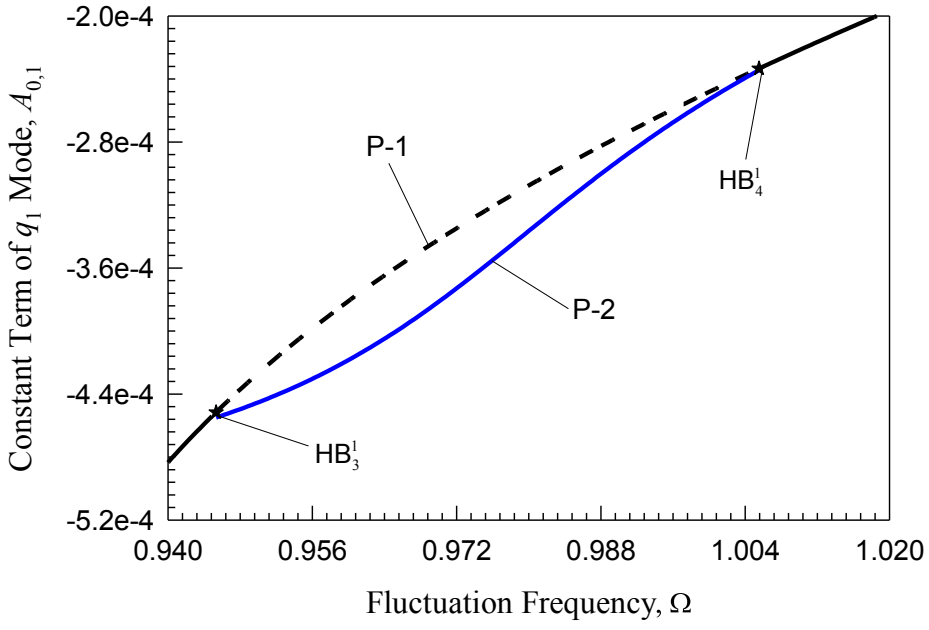

(d)

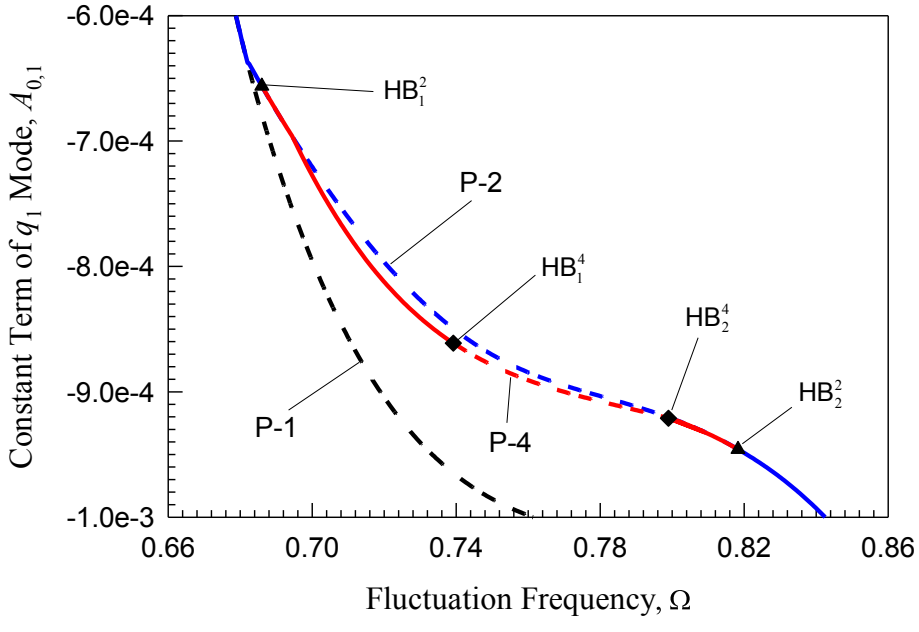

(e)

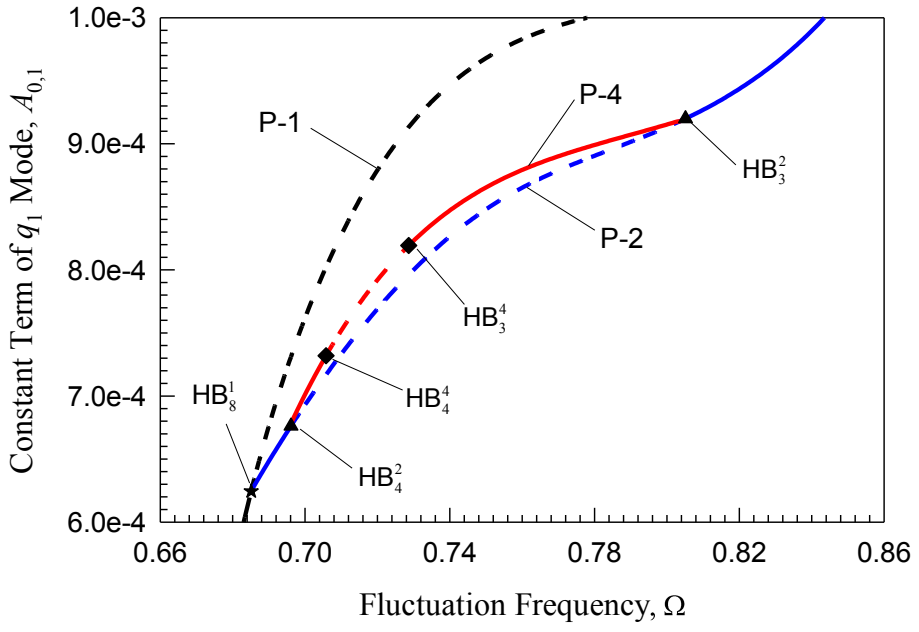

(f)

Fig.4 Constant term's amplitude $A_{0,1}$ of the bending mode: (b), (c) and (e) are the partially zoom in on the lower branch of (a). (d) and (f) are the partially zoom in on the upper branch of (a). (a) to (d) represent for period-1 and period-2. (e) to (f) are for period-1, period-2 and period-4. ($E = 69\text{GMa}$, $\rho = 2712\text{kg/m}^3$, $A = 0.0002\text{m}^2$, $J = 2.5\times10^{-9}m^4$, $L = 1.5\text{m}$).

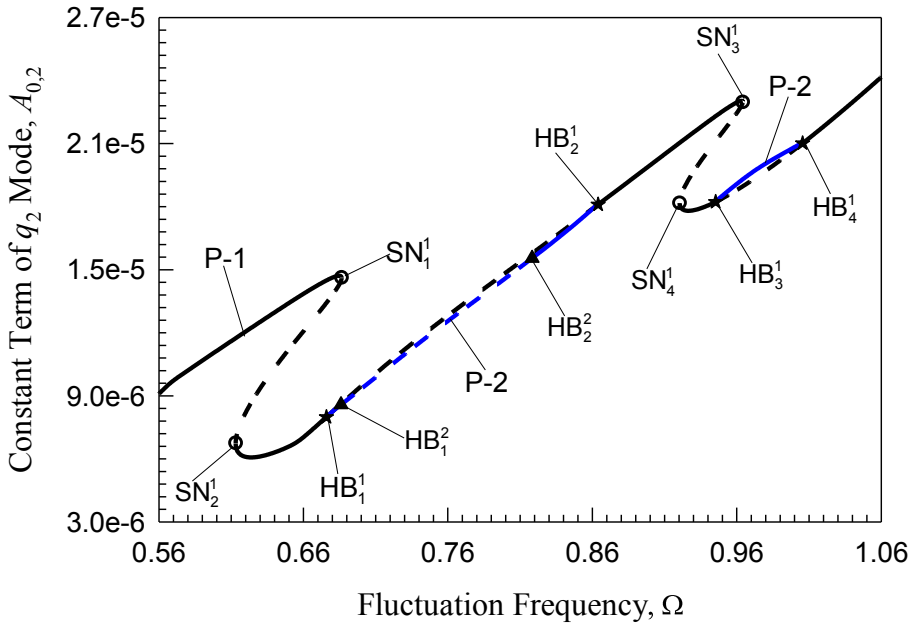

(a)

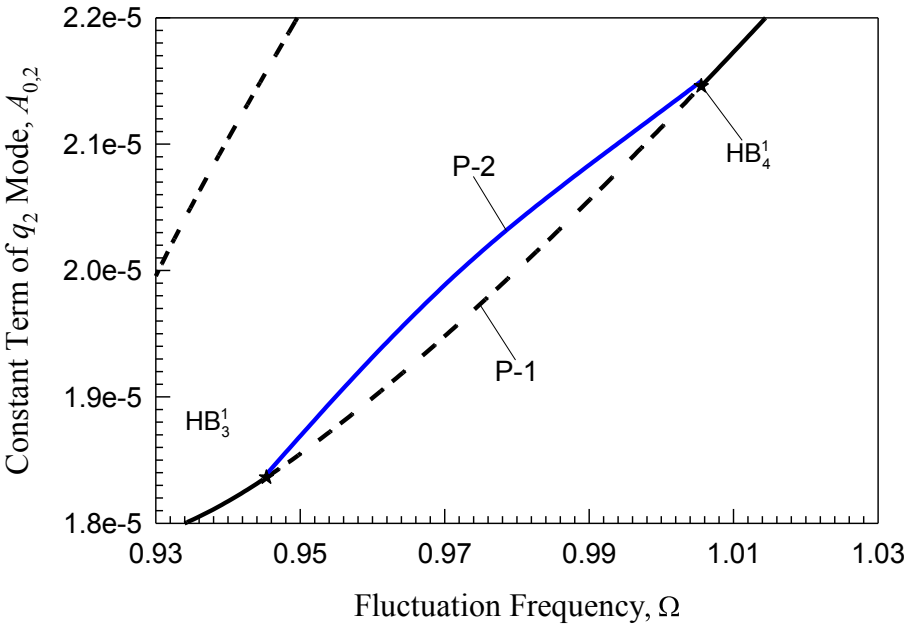

(b)

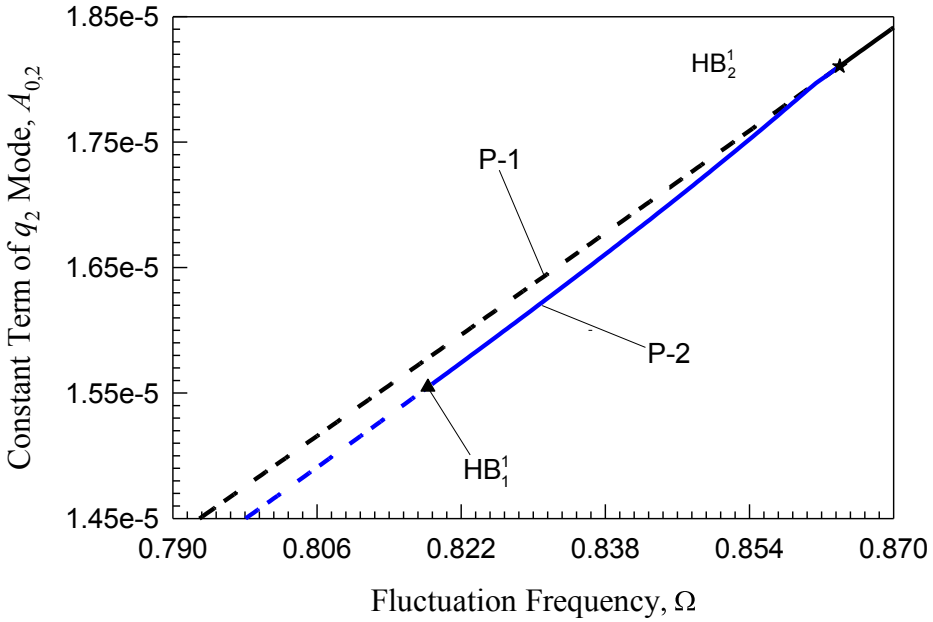

(c)

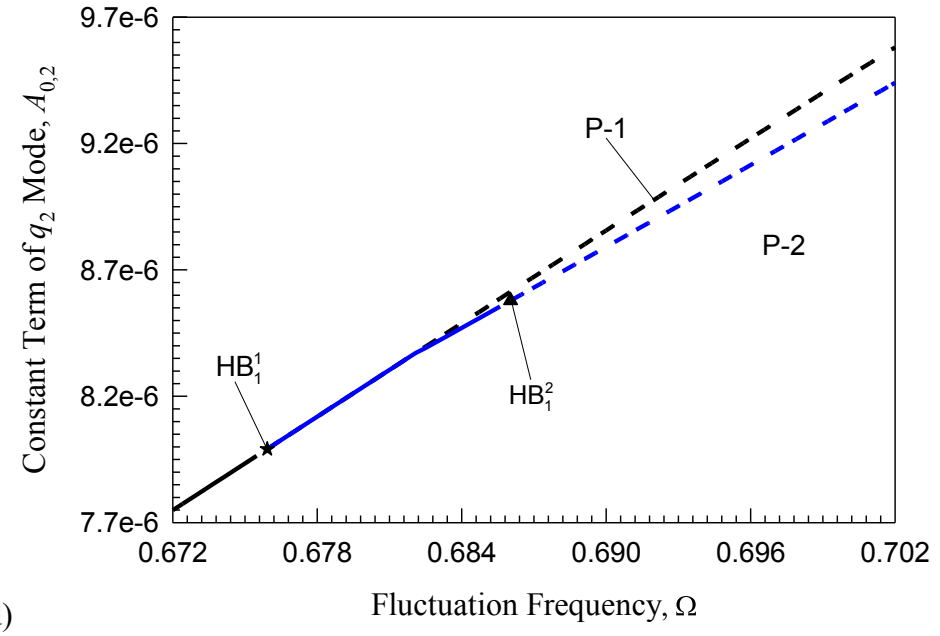

(d)

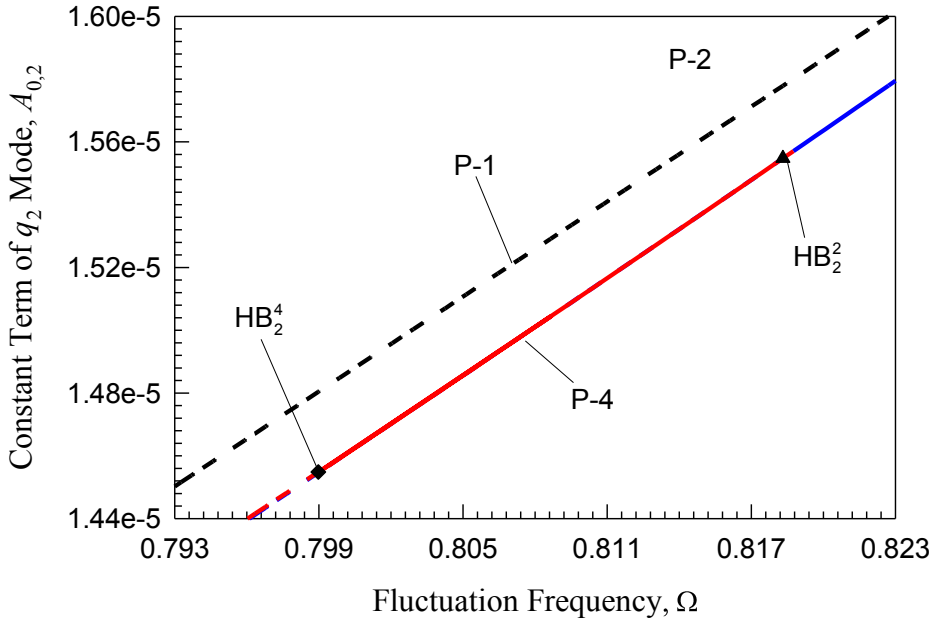

(e)

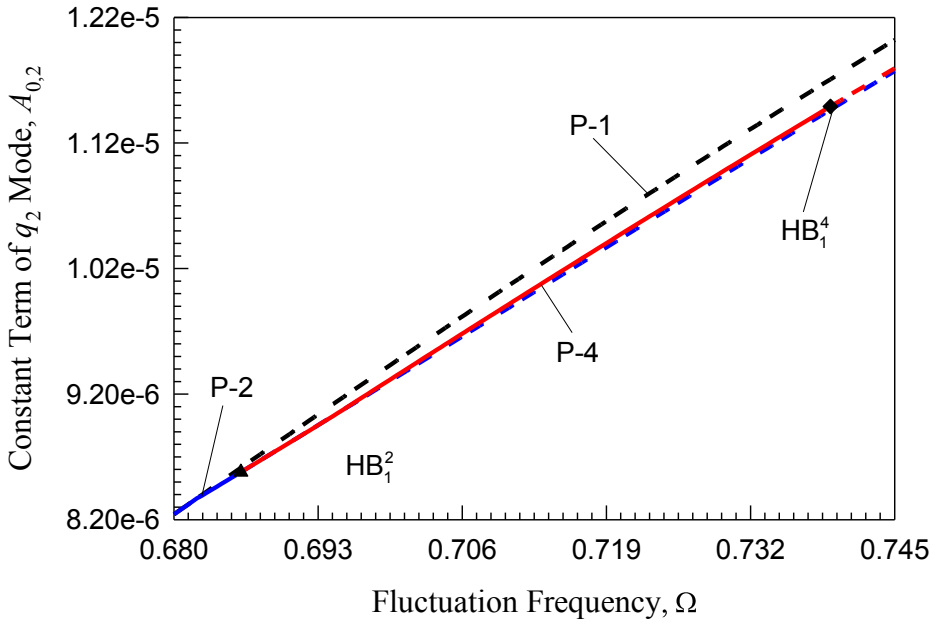

(f)

Fig.5 Constant term's amplitude $A_{0,2}$ of the axial mode for the lower branch: (b) to (f) are the partially zoom in of (a). (a) to (d) represent for period-1 and period-2. (e) to (f) are for period-1, period-2 and period-4. ($E = 69\text{GMa}$, $\rho = 2712\text{kg/m}^3$, $A = 0.0002\text{m}^2$, $J = 2.5\times10^{-9}\text{m}^4$, $L = 1.5\text{m}$).

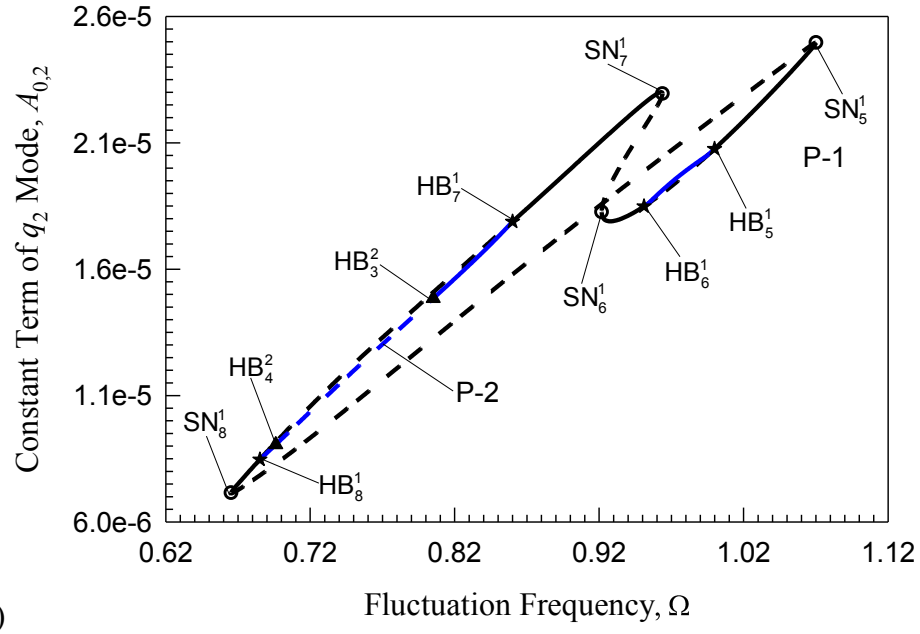

(a)

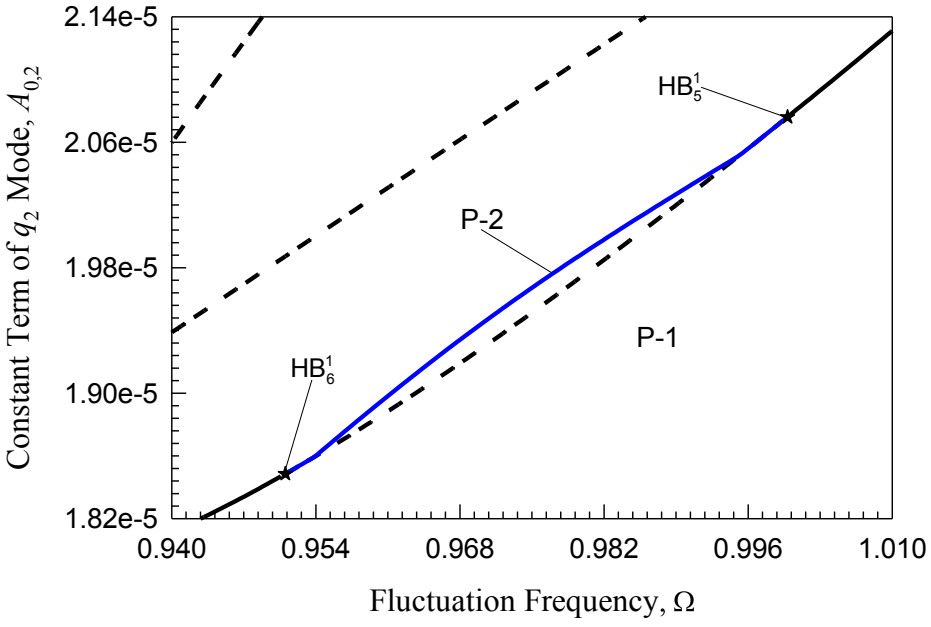

(b)

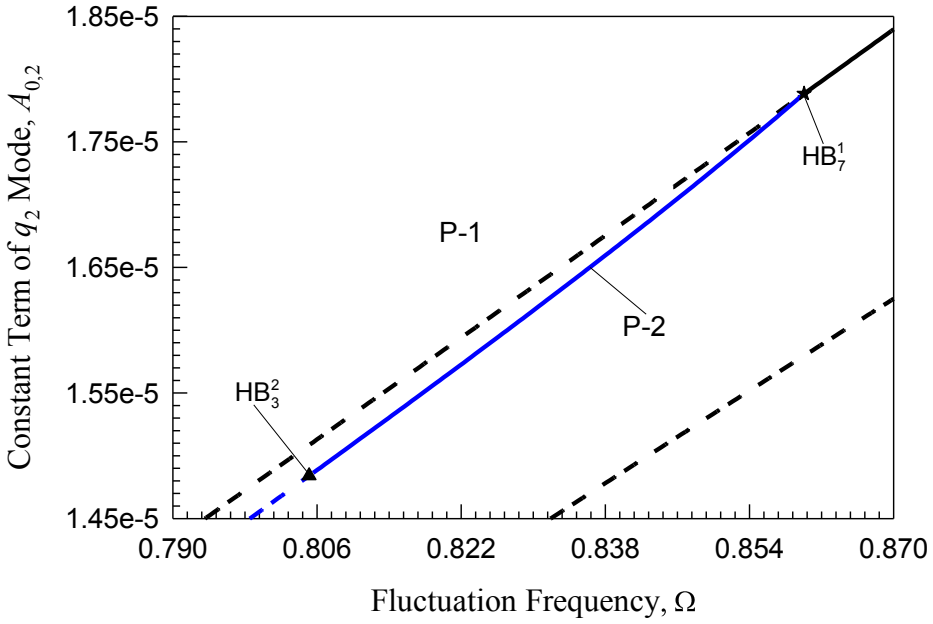

(c)

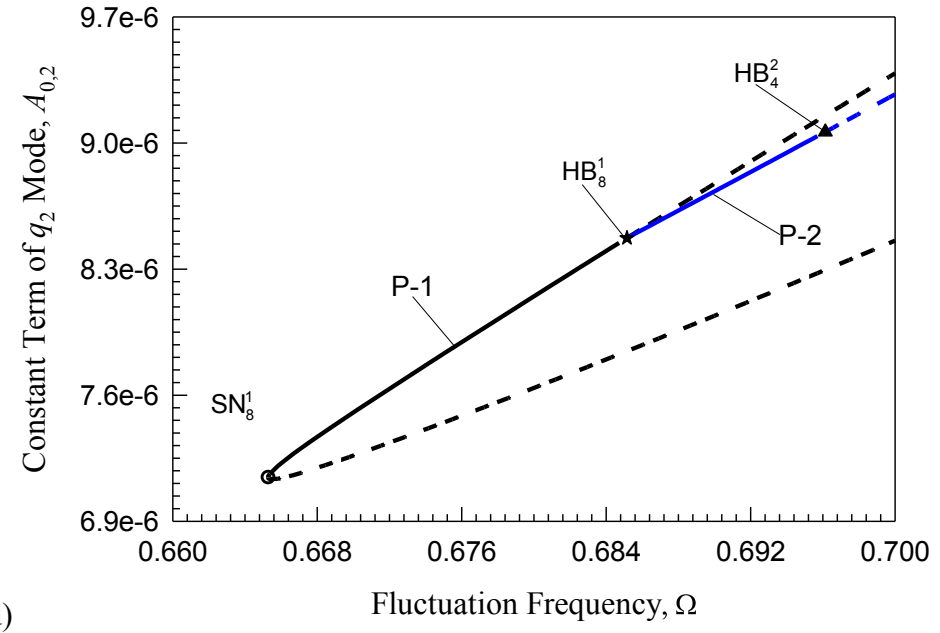

(d)

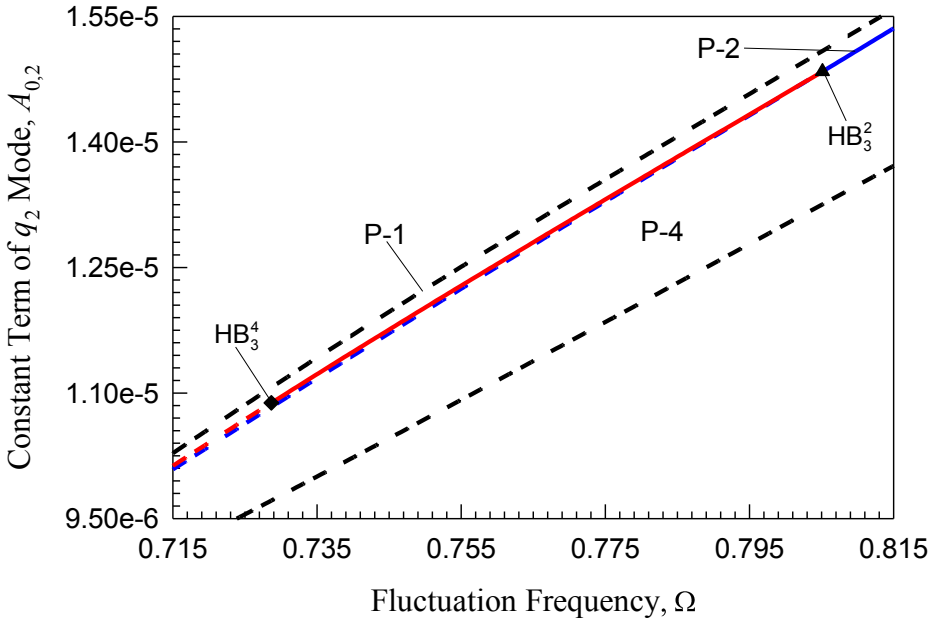

(e)

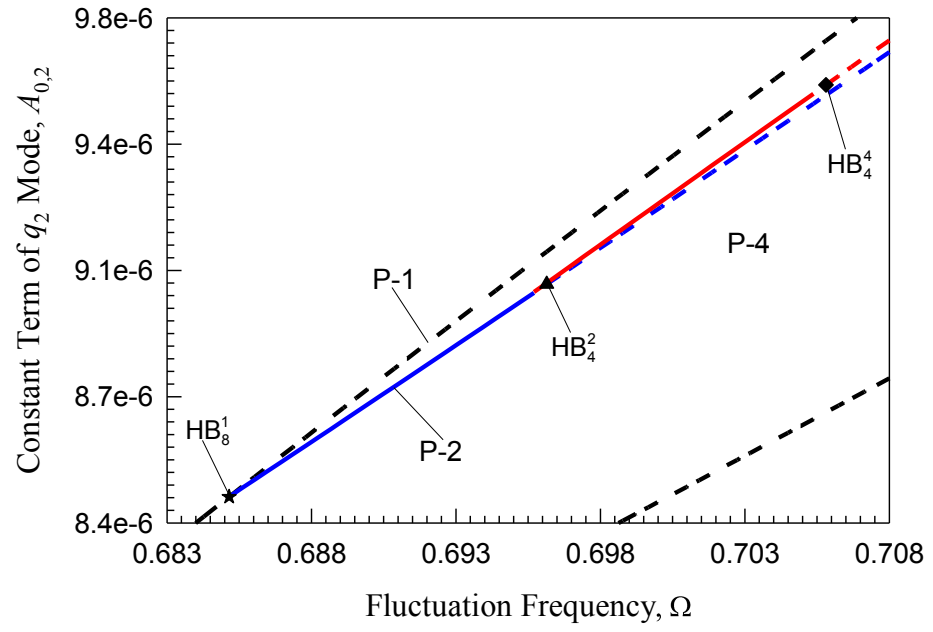

(f)

Fig.6 Constant term's amplitude $A_{0,2}$ of the axial mode for the upper branch: (b) to (f) are the partially zoom in of (a). (a) to (d) represent for period-1 and period-2. (e) to (f) are for period-1, period-2 and period-4. ($E = 69\text{GMa}$, $\rho = 2712\text{kg/m}^3$, $A = 0.0002\text{m}^2$, $J = 2.5\times10^{-9}\text{m}^4$, $L = 1.5\text{m}$).

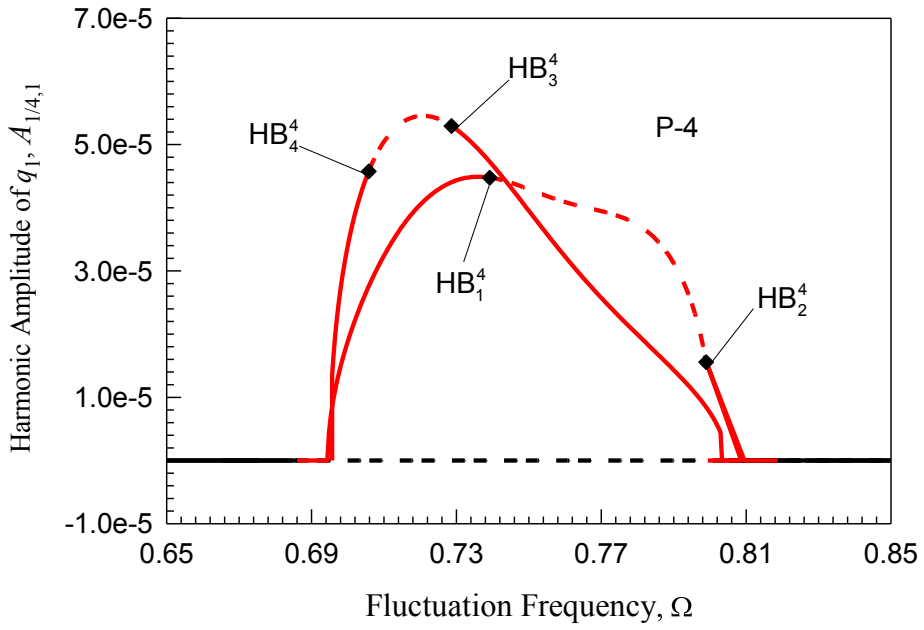

(a)

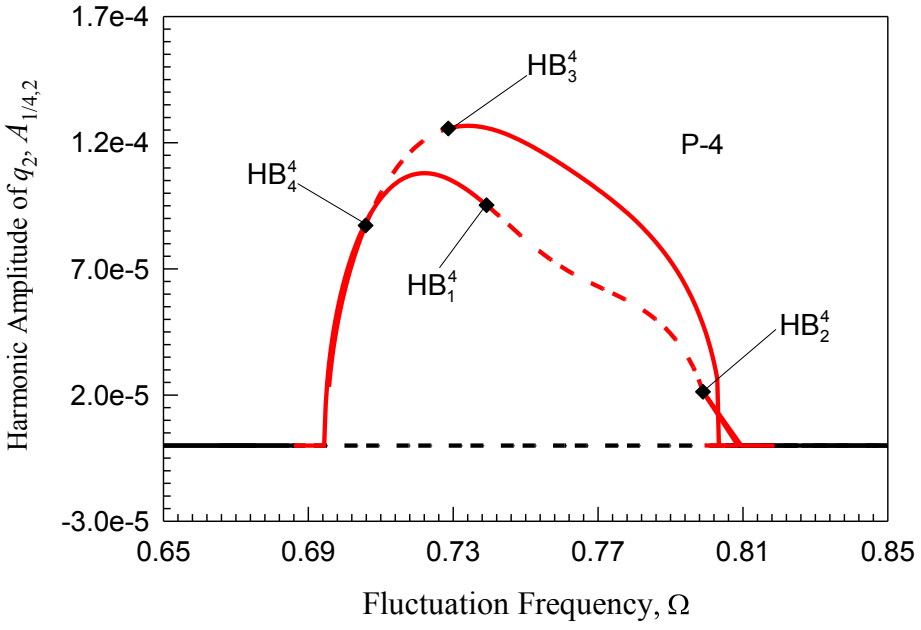

(b)

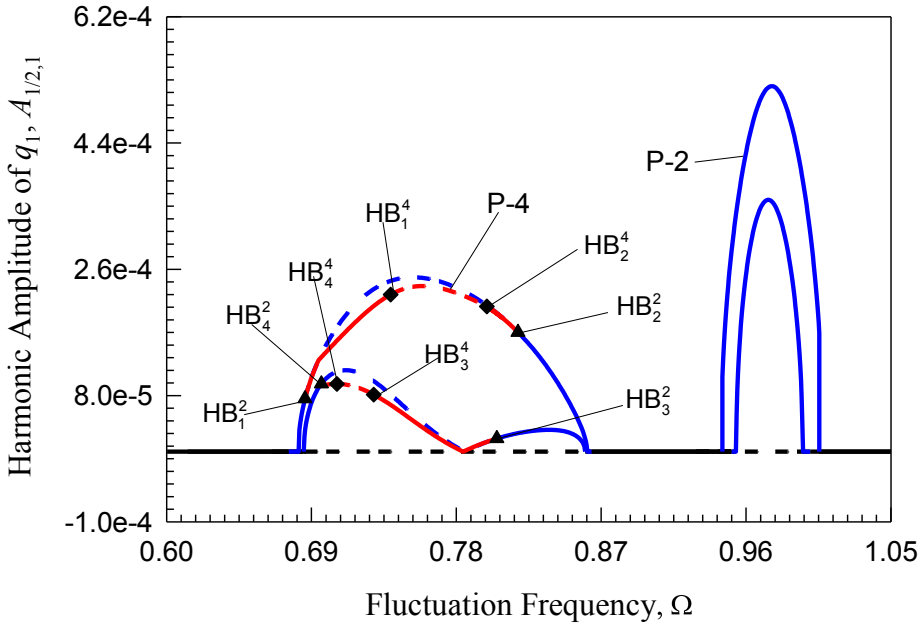

(c)

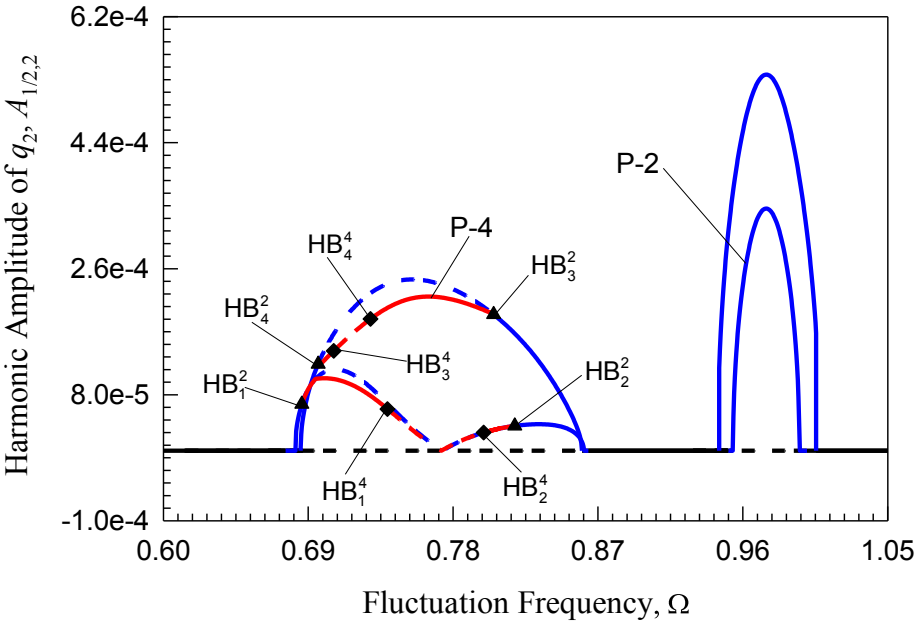

(d)

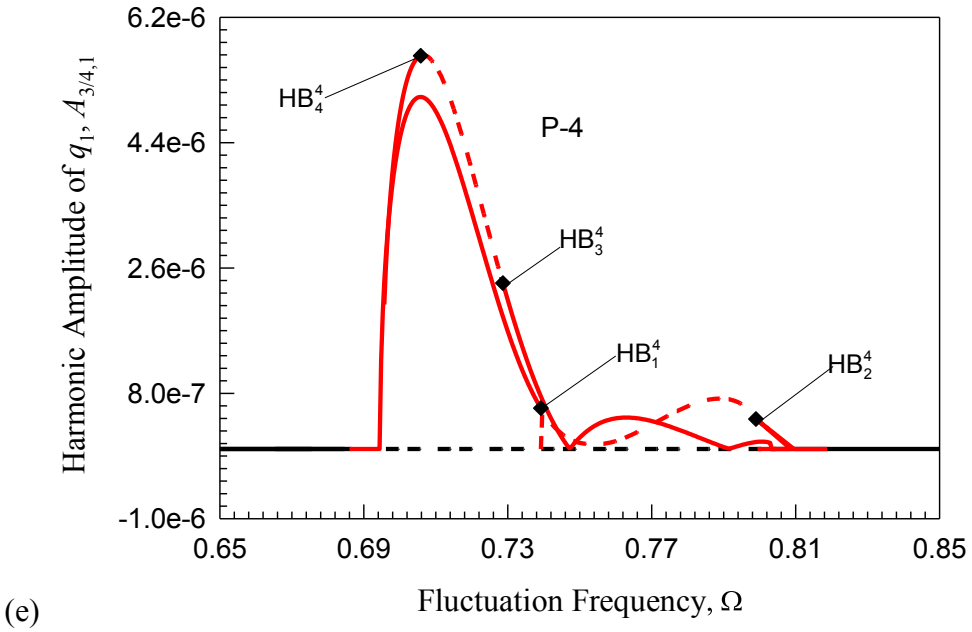

(e)

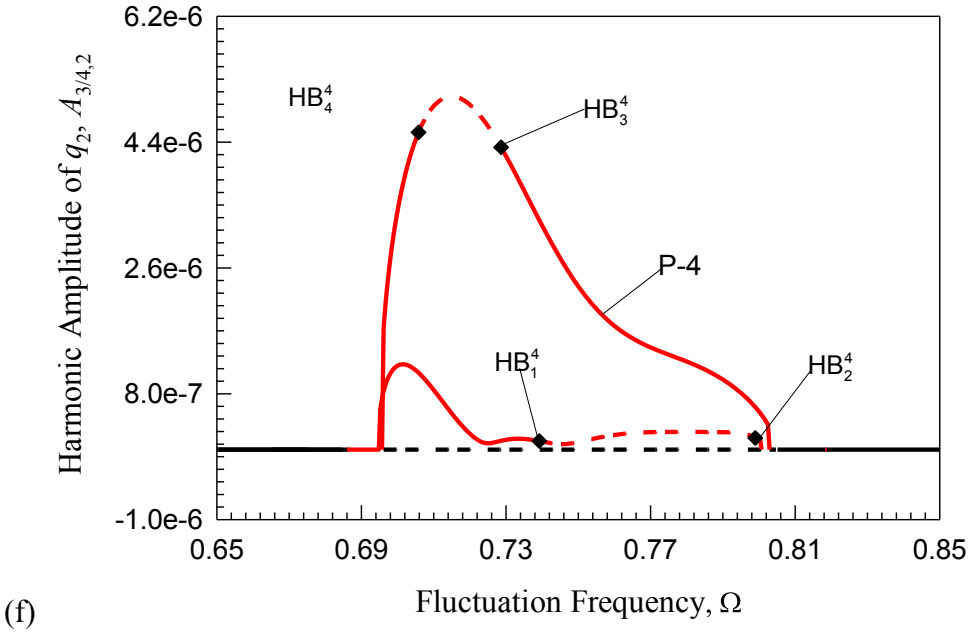

(f)

Fig.7 Fraction terms' amplitude for both bending and axial modes: (a), (c) and (e) are harmonic amplitude of bending mode $A_{1/4,1}$, $A_{1/2,1}$, $A_{3/4,1}$; (b), (d) and (f) are harmonic amplitude of axial mode $A_{1/4,2}$, $A_{1/2,2}$, $A_{3/4,2}$. ($E = 69\text{GMa}$, $\rho = 2712\text{kg/m}^3$, $A = 0.0002\text{m}^2$, $J = 2.5\times10^{-9}\text{m}^4$, $L = 1.5\text{m}$).

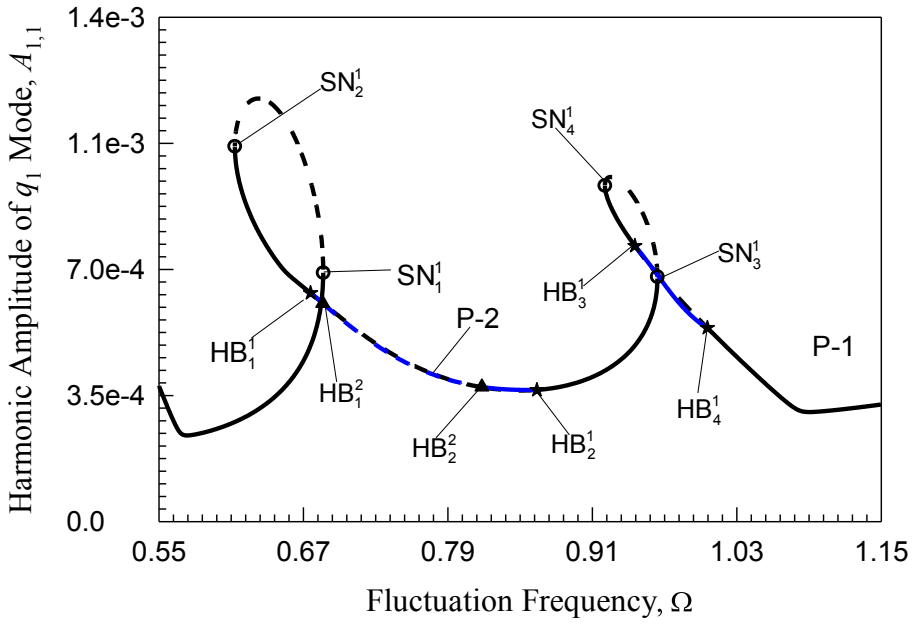

(a)

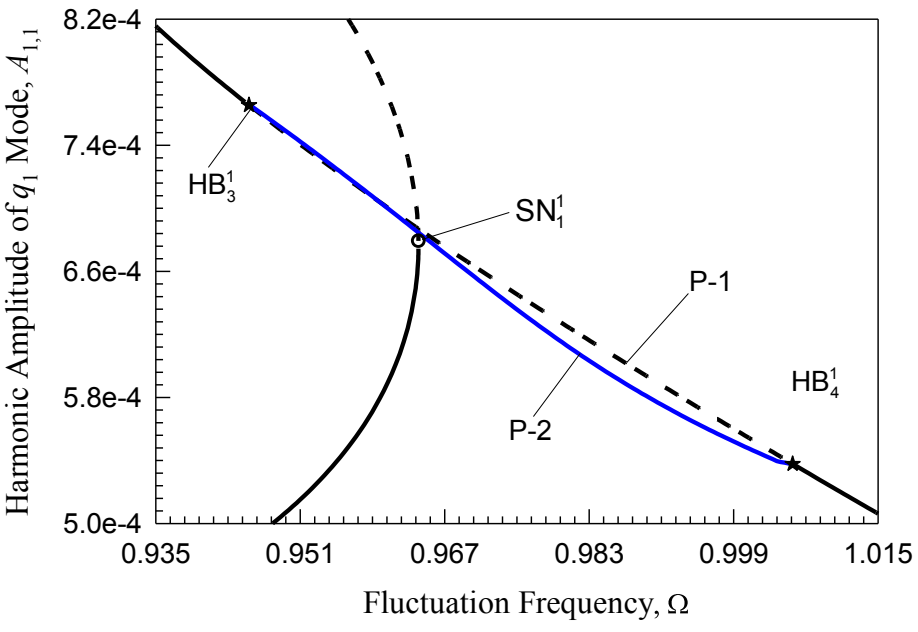

(b)

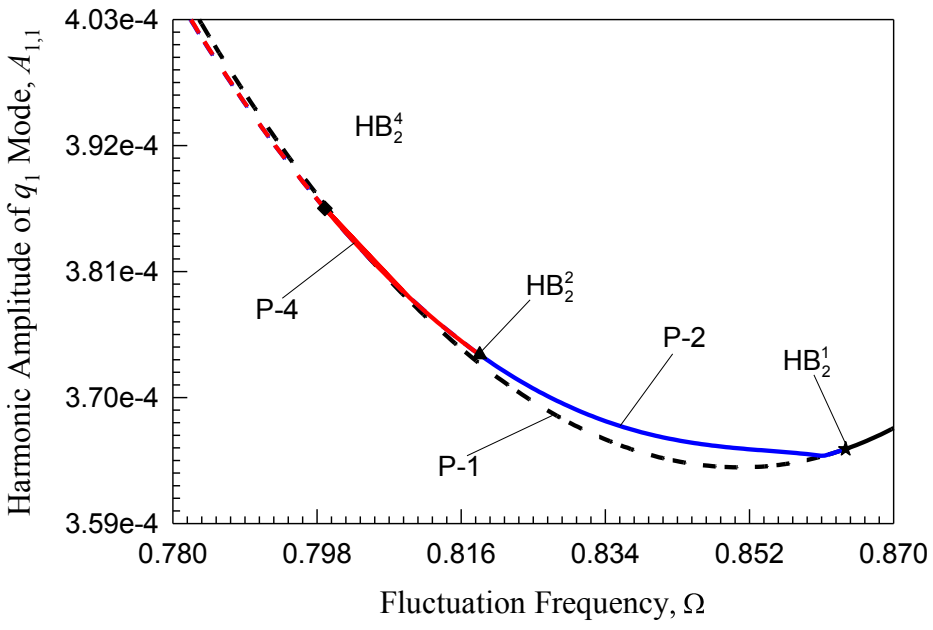

(c)

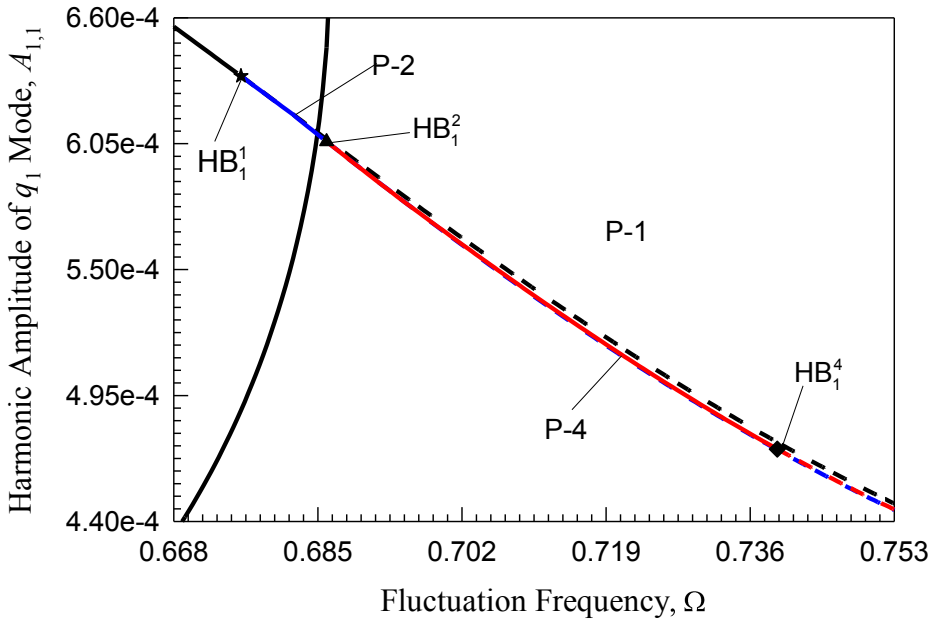

(d)

Fig.8 First Harmonic term's amplitude $A_{1,1}$ of the bending mode for the lower branch: (b), (c), and (d) are the partially zoom in of (a). (a) and (b) represent for period-1 and period-2. (c) and (f) present for period-1, period-2 and period-4. ($E = 69\text{GMa}$, $\rho = 2712\text{kg/m}^3$, $A = 0.0002\text{m}^2$, $J = 2.5\times10^{-9} m^4$, $L = 1.5\text{m}$).

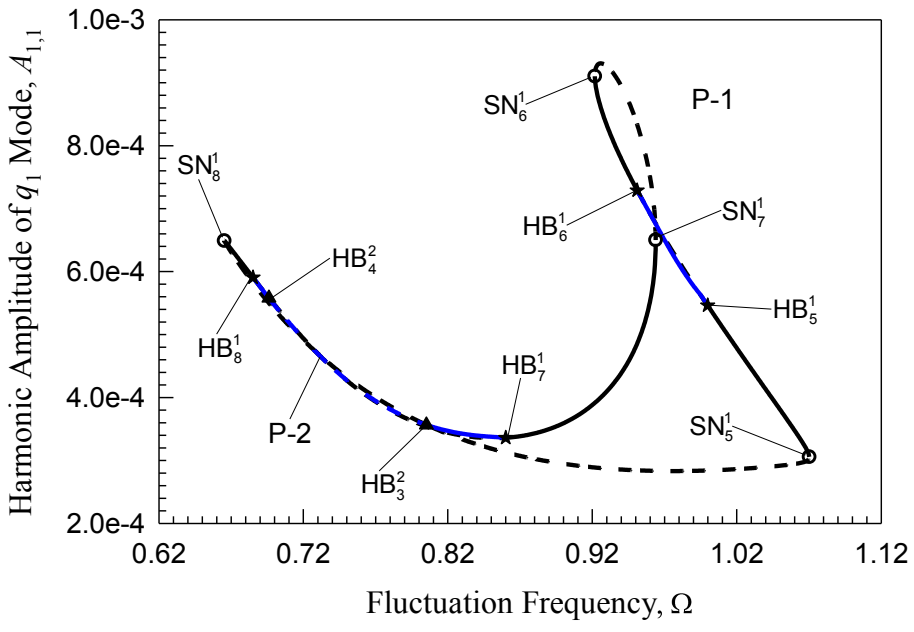

(a)

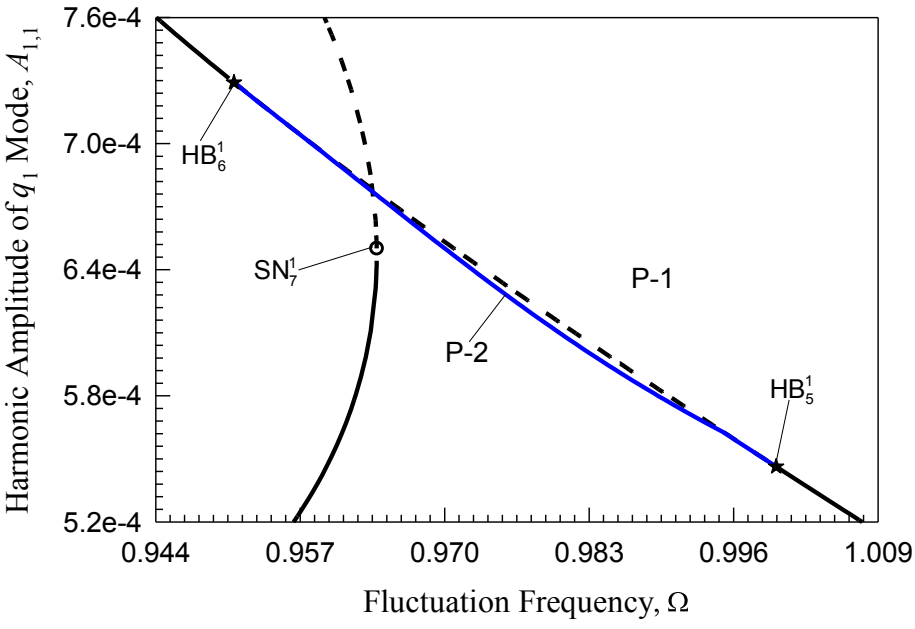

(b)

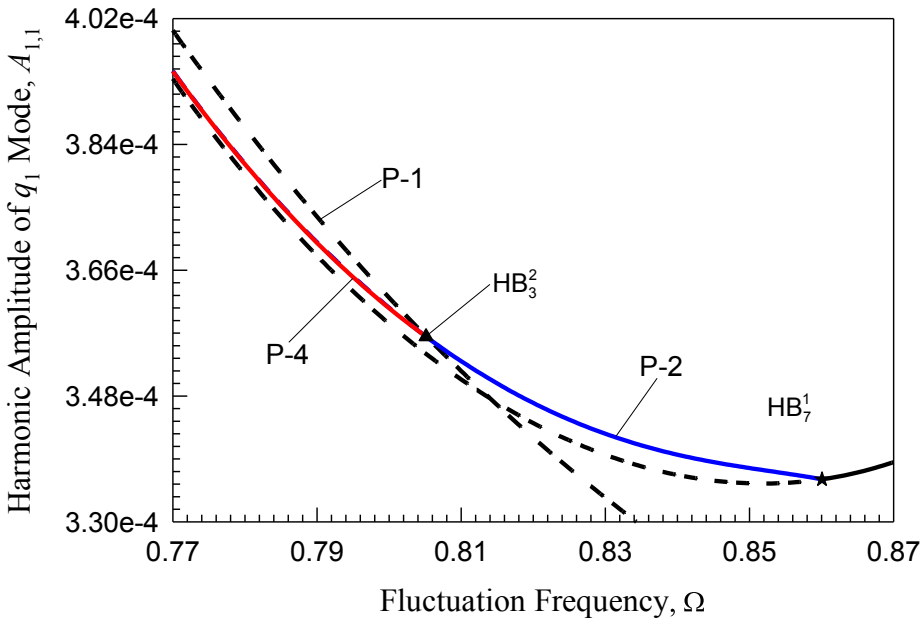

(c)

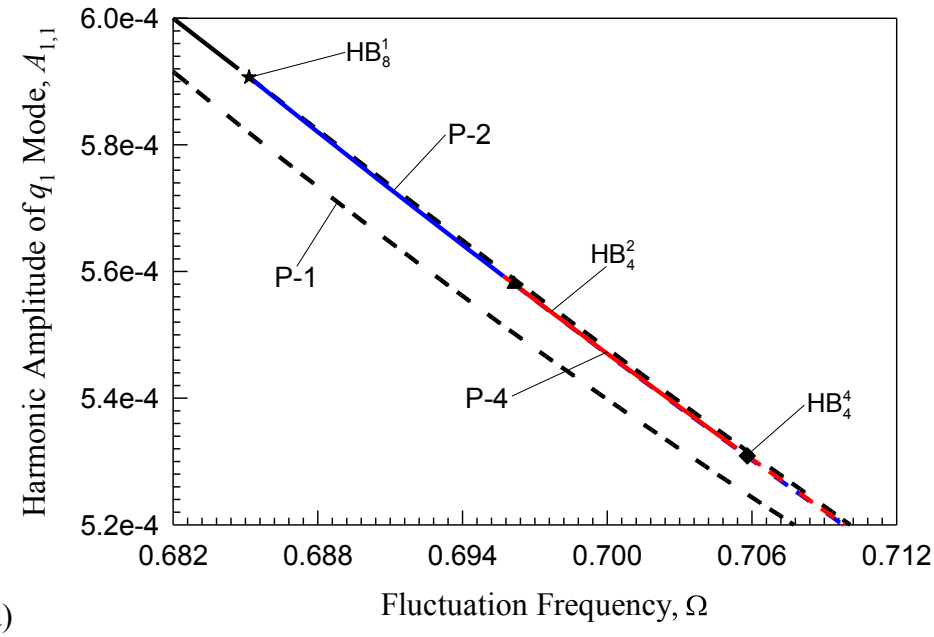

(d)

Fig.9 First Harmonic term's amplitude $A_{1,1}$ of the bending mode for the upper branch: (b), (c), and (d) are the partially zoom in of (a). (a) and (b) represent for period-1 and period-2. (c) and (f) present for period-1, period-2 and period-4. ($E = 69\text{GMa}$, $\rho = 2712\text{kg/m}^3$, $A = 0.0002\text{m}^2$, $J = 2.5\times10^{-9} m^4$, $L = 1.5\text{m}$).

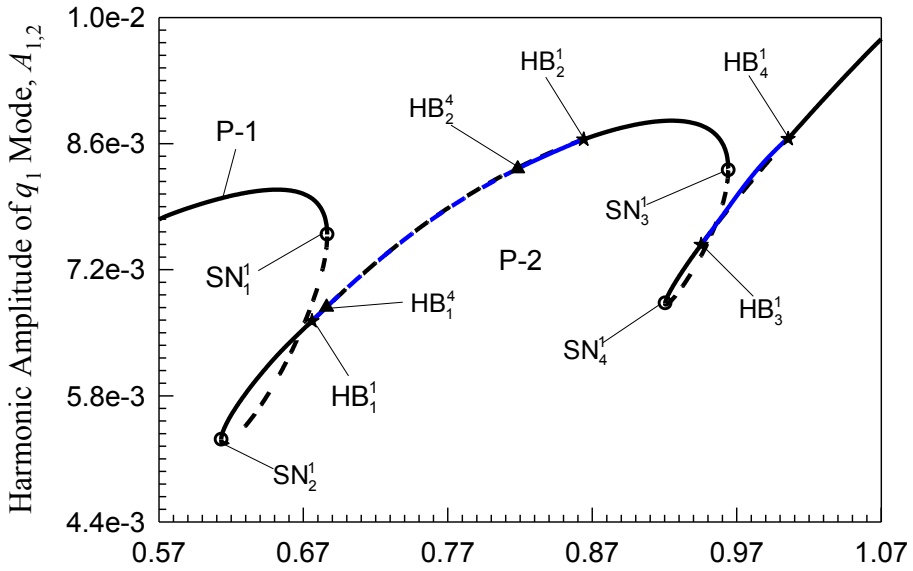

(a)

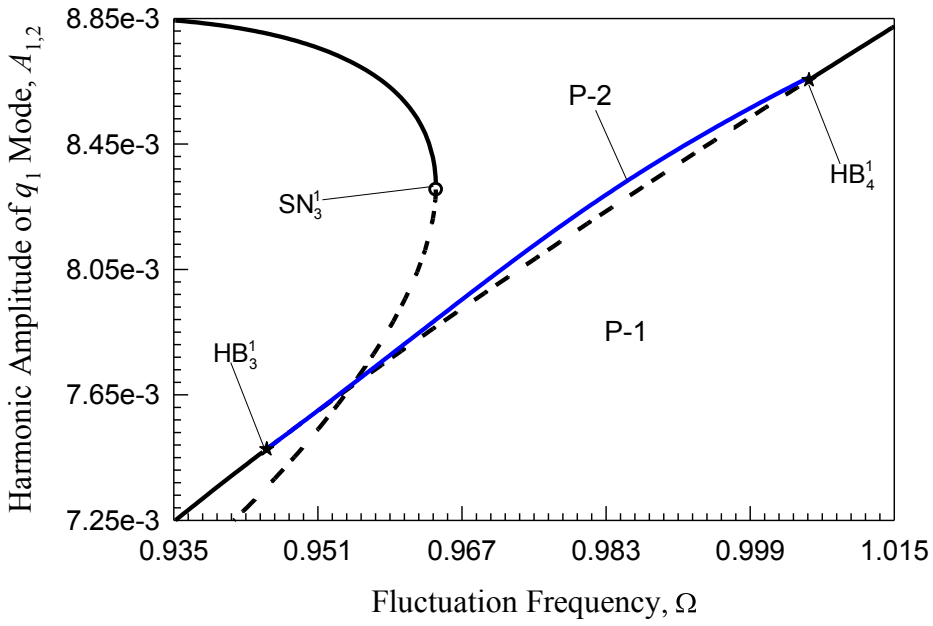

(b)

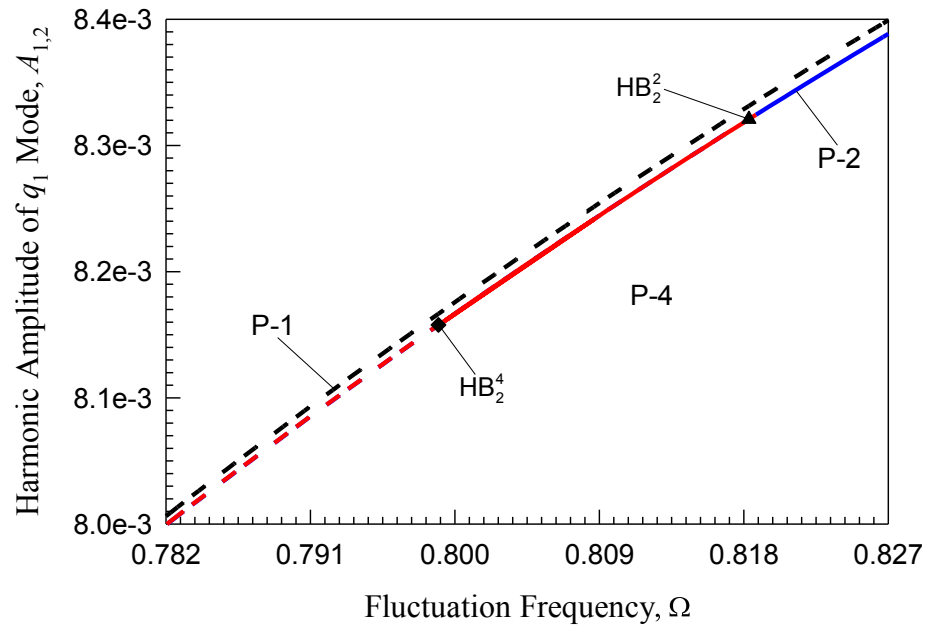

(c)

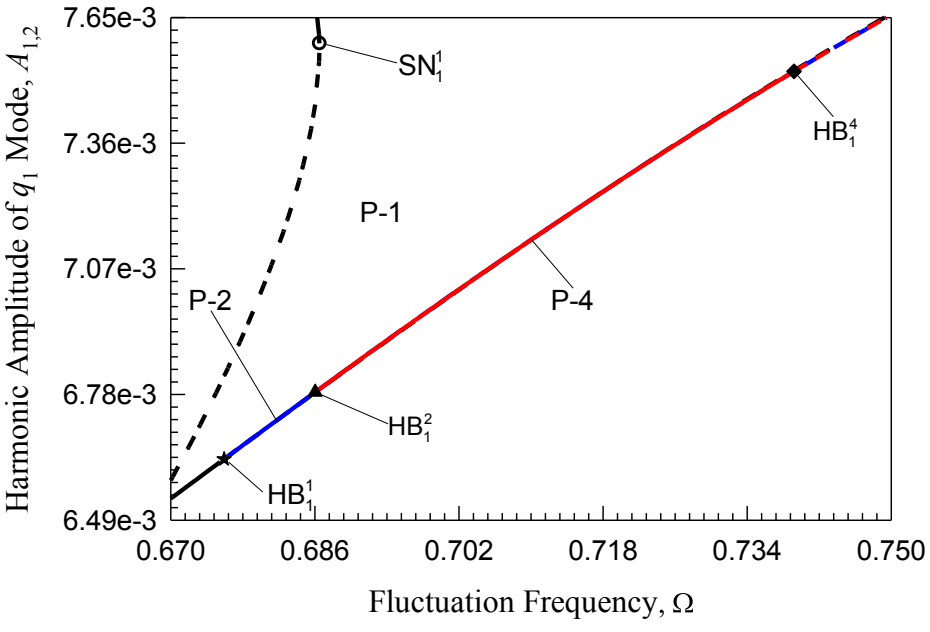

(d)

Fig.10 First Harmonic term's amplitude $A_{1,2}$ of the axial mode for the lower branch: (b), (c), and (d) are the partially zoom in of (a). (a) and (b) represent for period-1 and period-2. (c) and (f) present for period-1, period-2 and period-4. ($E = 69\text{GMa}$, $\rho = 2712\text{kg/m}^3$, $A = 0.0002\text{m}^2$, $J = 2.5\times10^{-9} m^4$, $L = 1.5\text{m}$).

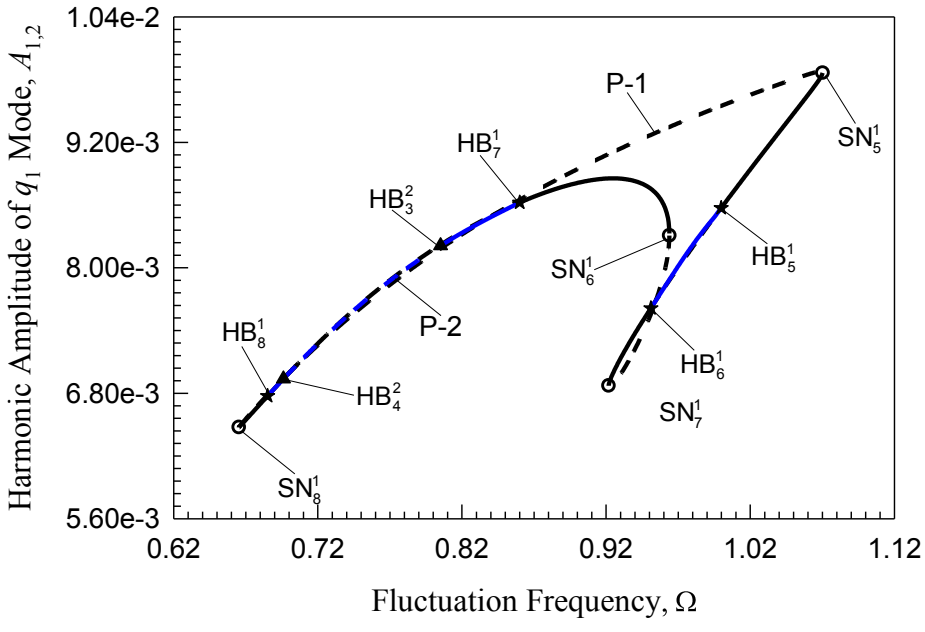

(a)

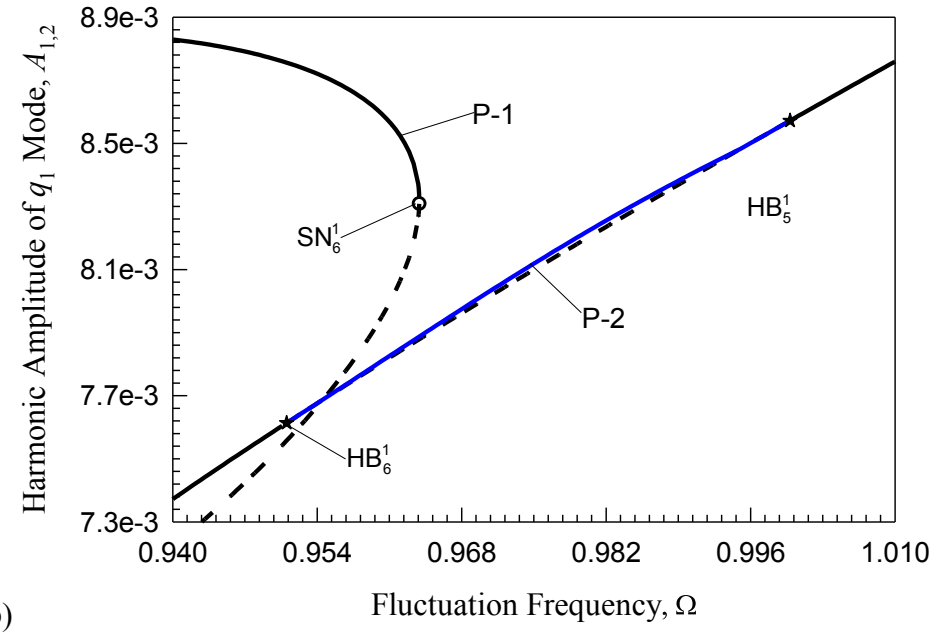

(b)

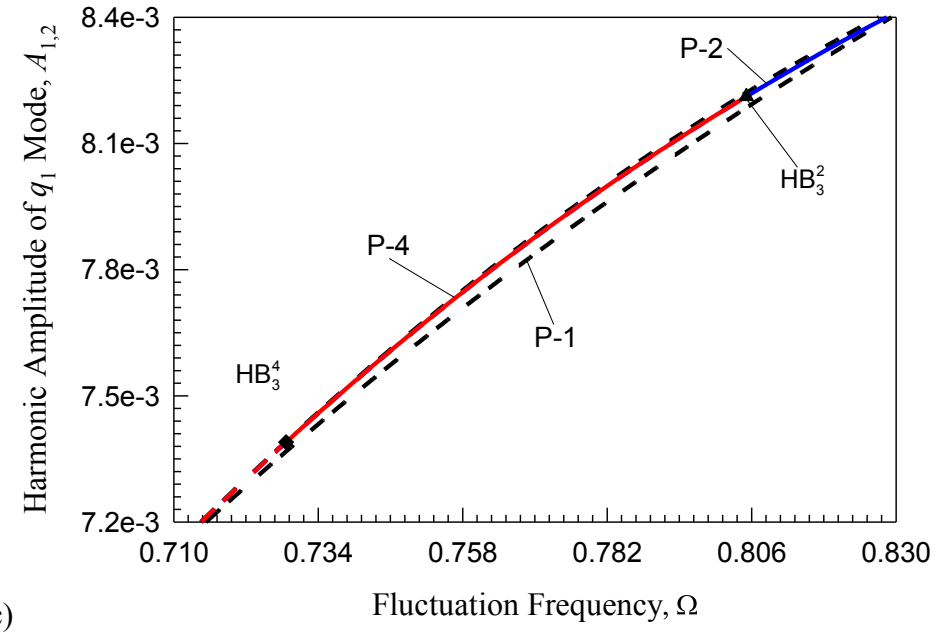

(c)

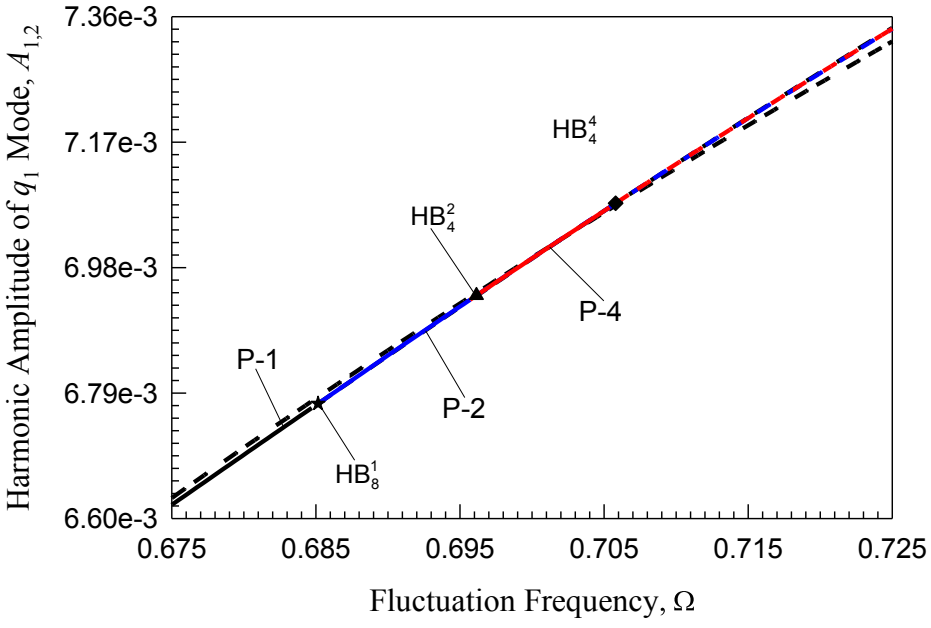

(d)

Fig.11 First Harmonic term's amplitude $A_{1,2}$ of the axial mode for the upper branch: (b), (c), and (d) are the partially zoom in of (a). (a) and (b) represent for period-1 and period-2. (c) and (f) present for period-1, period-2 and period-4. ($E = 69\text{GMa}$, $\rho = 2712\text{kg/m}^3$, $A = 0.0002\text{m}^2$, $J = 2.5\times10^{-9}\text{m}^4$, $L = 1.5\text{m}$).

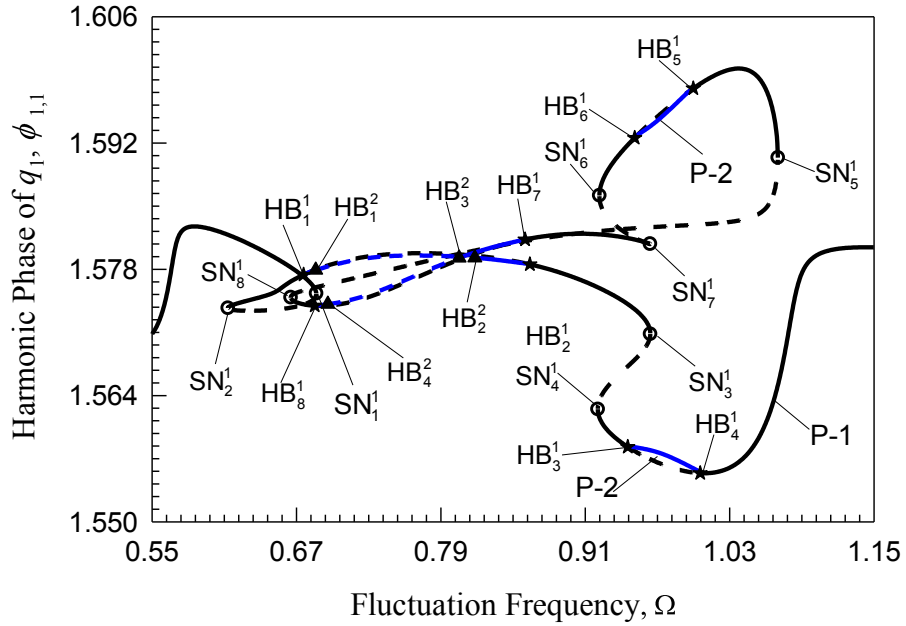

(a)

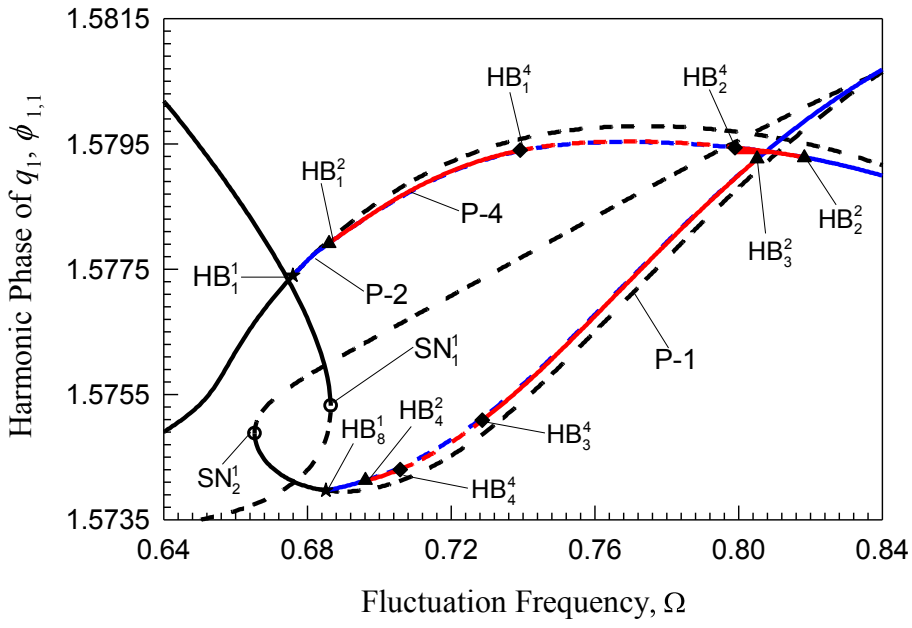

(b)

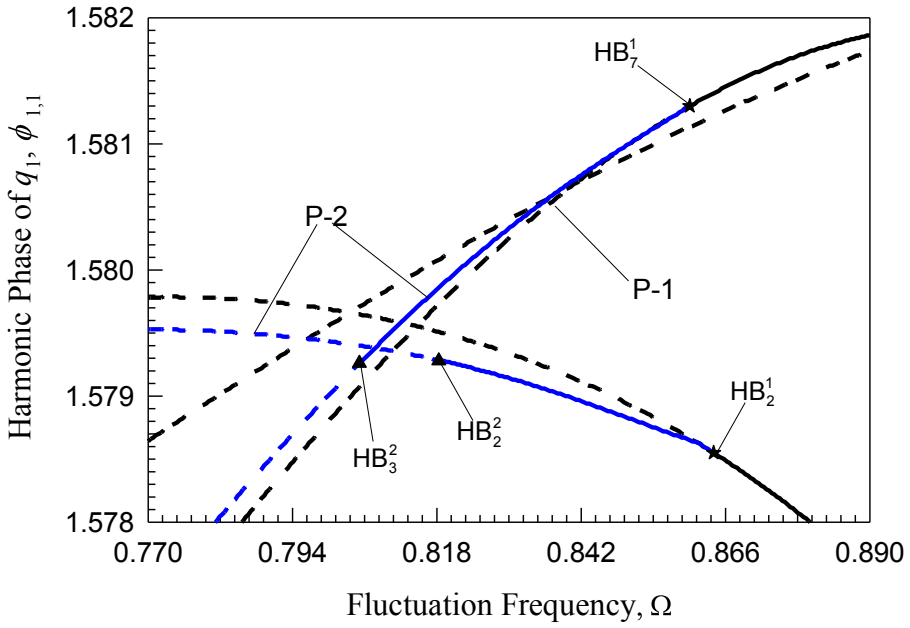

(c)

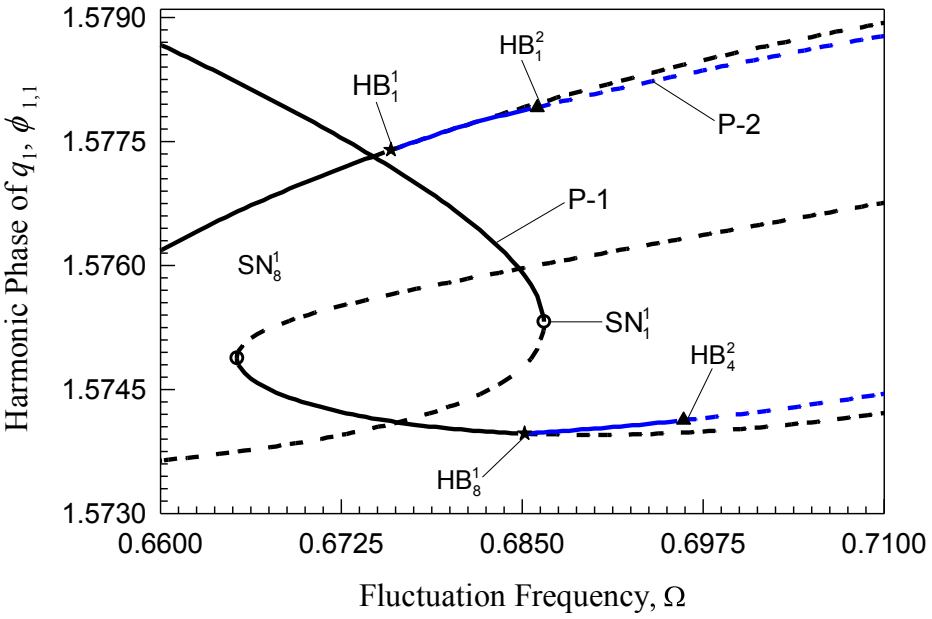

(d)

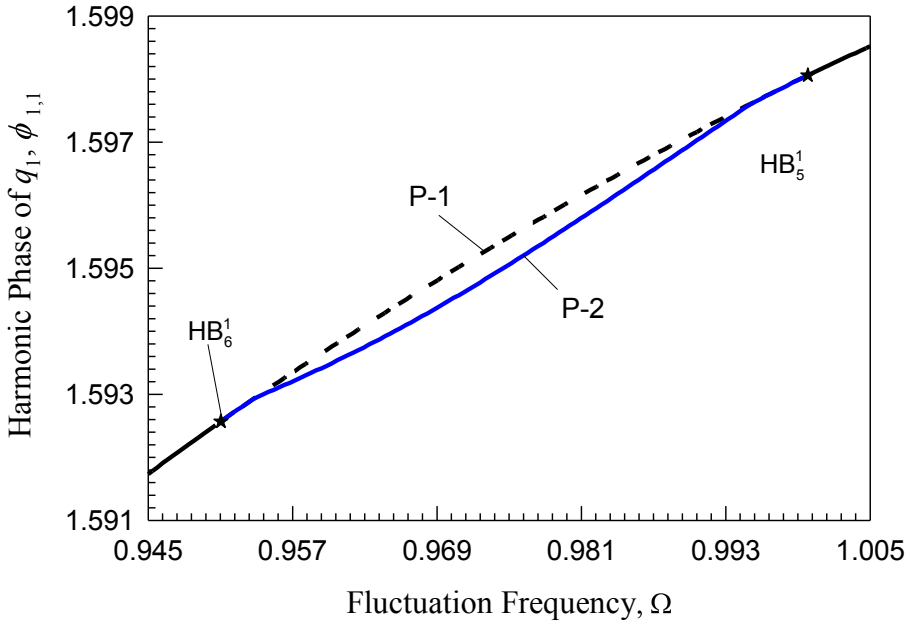

(e)

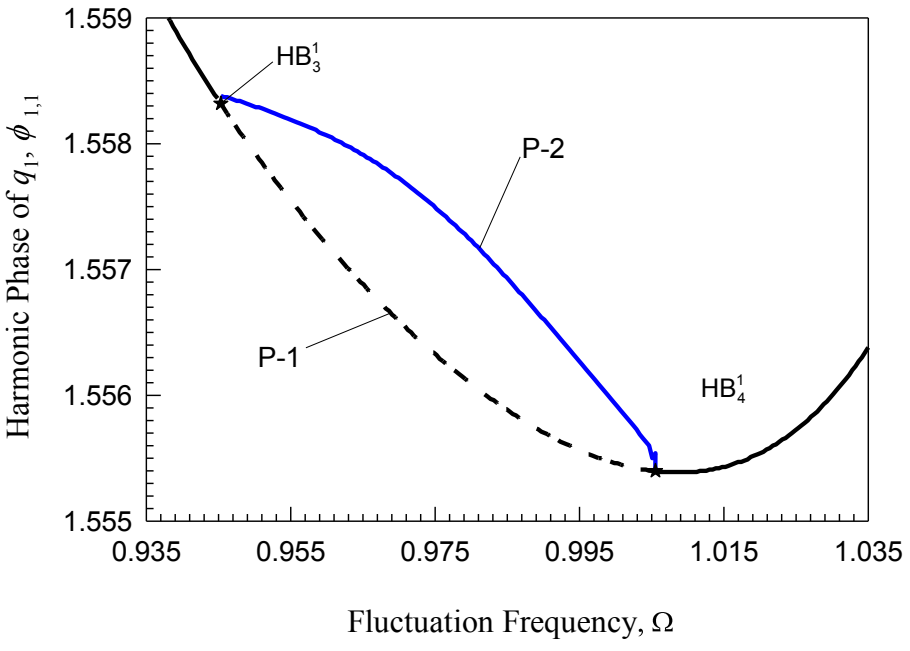

(f)

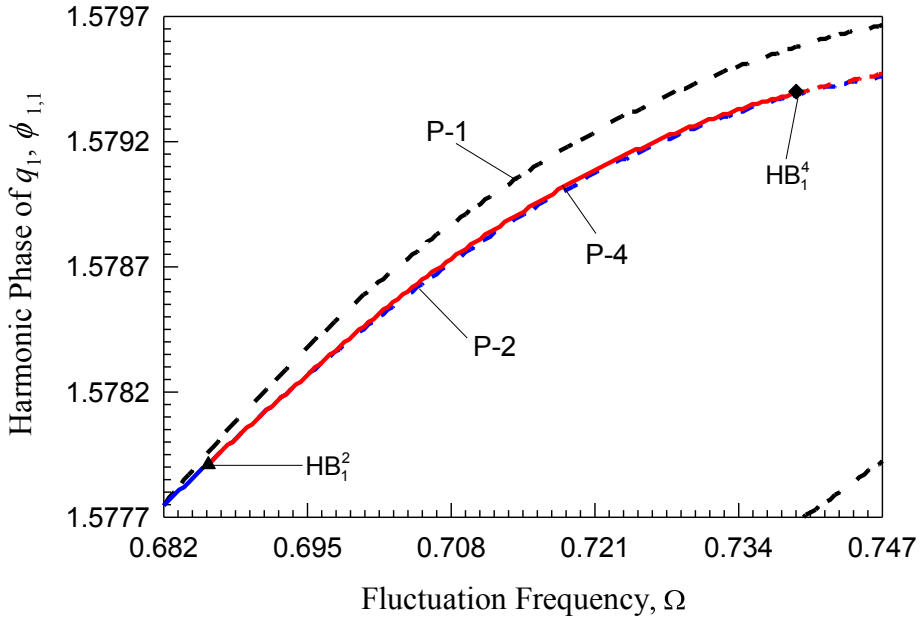

(g)

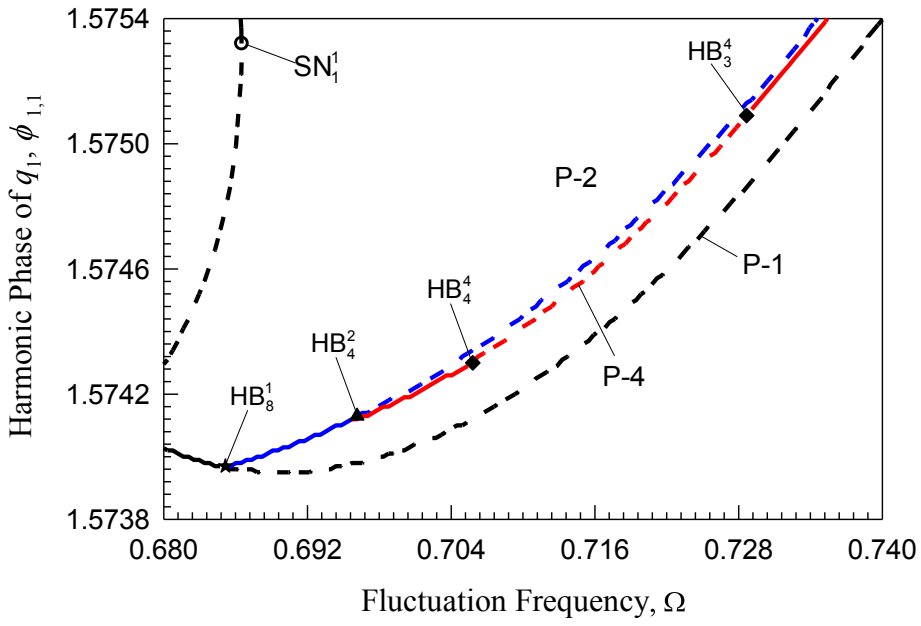

(h)

Fig.12 First Harmonic term's phase $\varphi_{1,1}$ of the bending mode: (b) - (h) are the partially zoom in on (a). (c) to (f) represent for period-1 and period-2. (b), (g) and (h) present for period-1, period-2 and period-4. ($E = 69\text{GMa}$, $\rho = 2712\text{kg/m}^3$, $A = 0.0002\text{m}^2$, $J = 2.5\times10^{-9}\text{m}^4$, $L = 1.5\text{m}$).

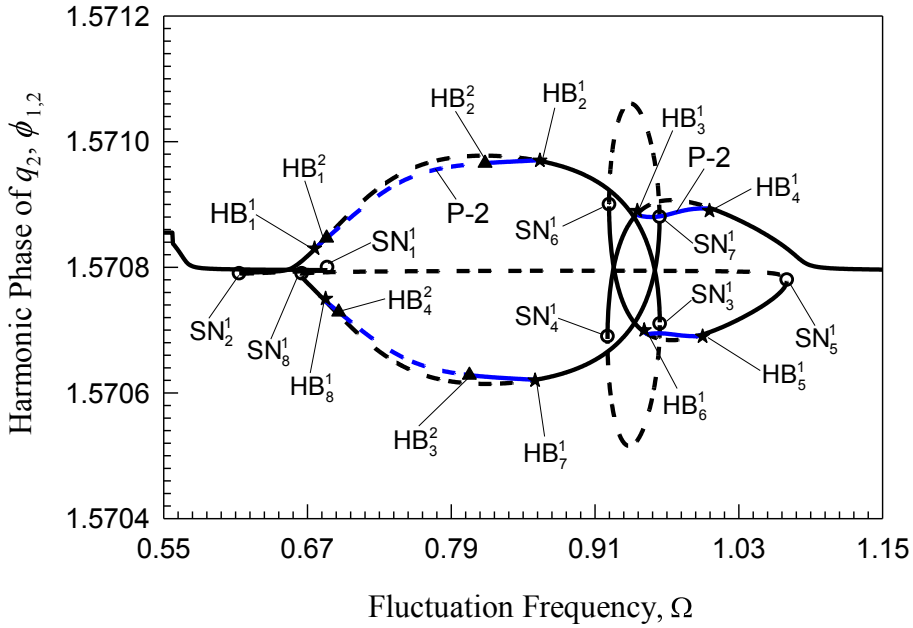

(a)

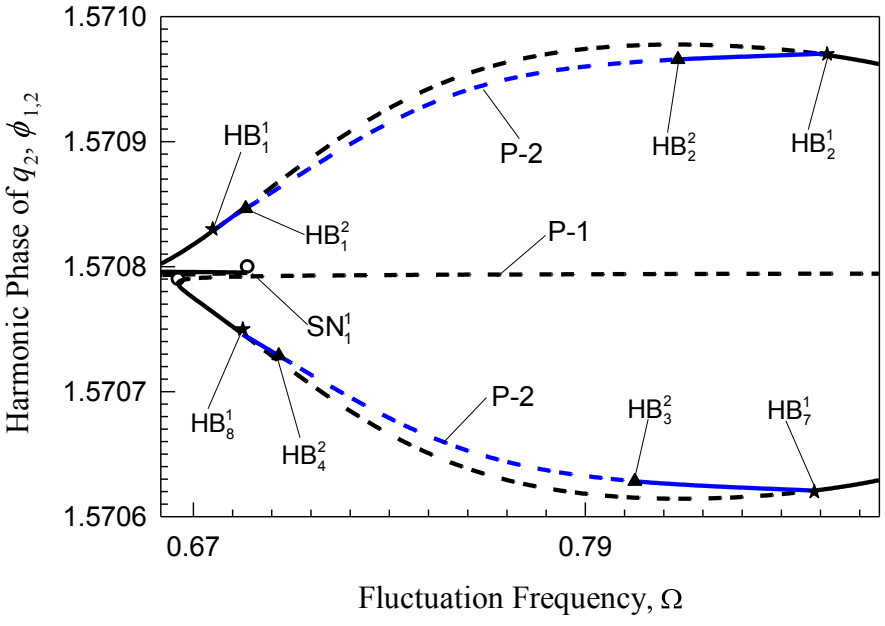

(b)

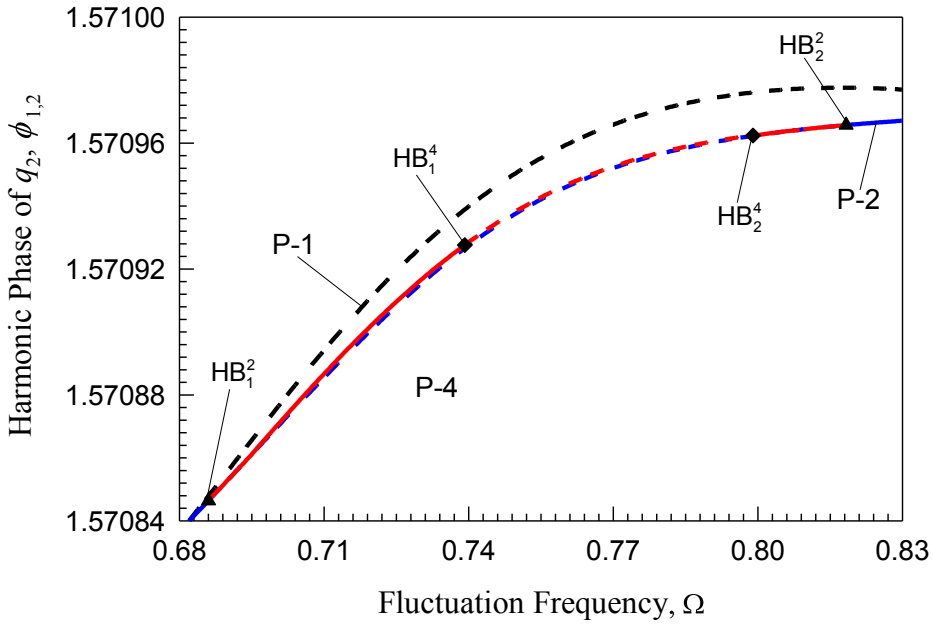

(c)

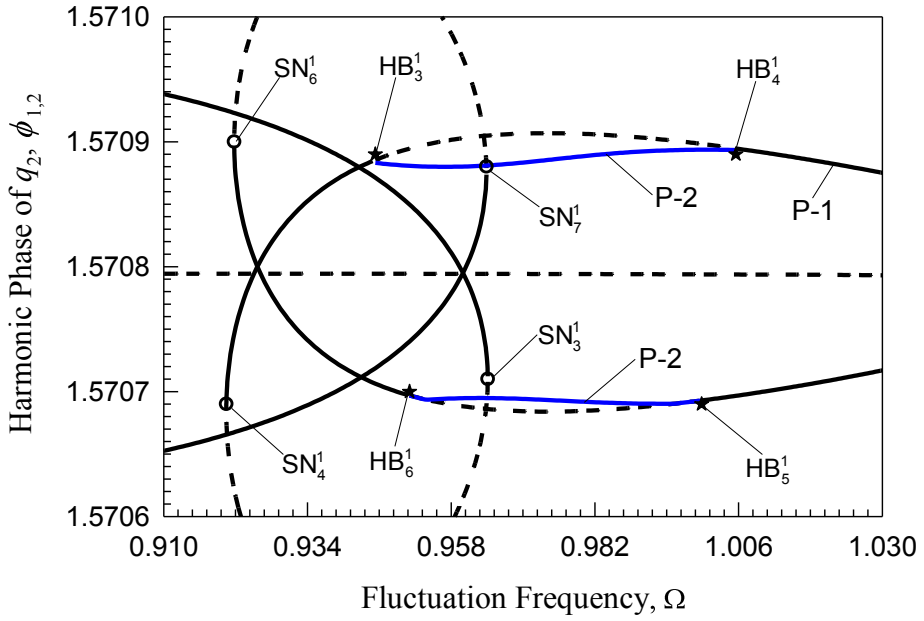

(d)

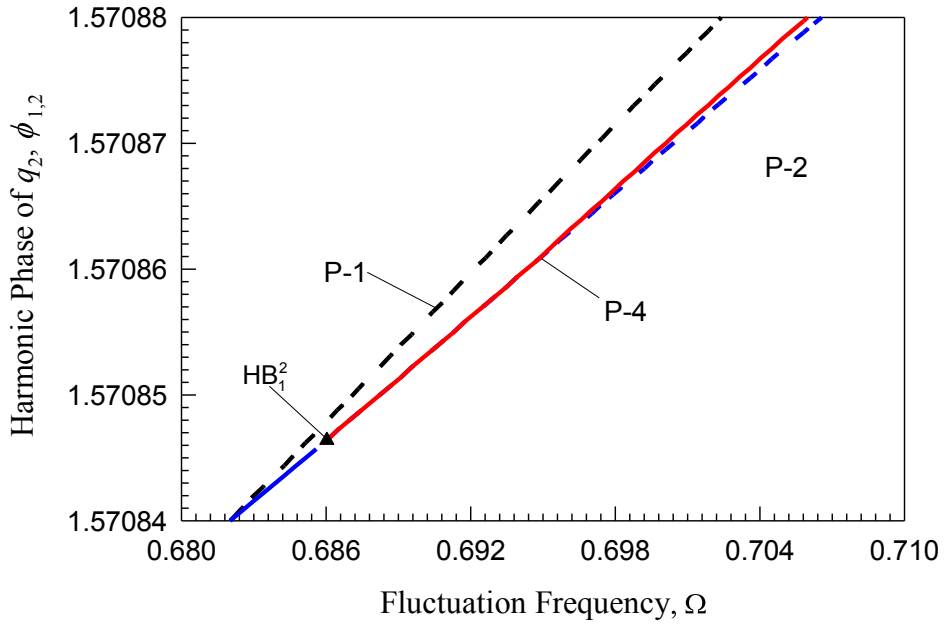

(e)

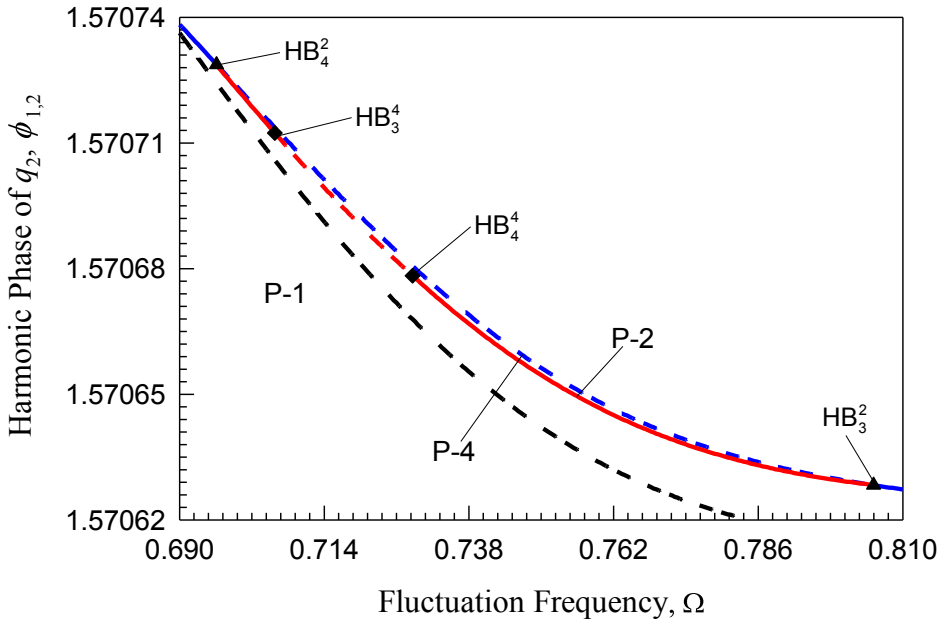

(f)

Fig.13 First Harmonic term's phase $\varphi_{1,2}$ of the axial mode: (b) - (h) are the partially zoom in on (a). (c) to (f) represent for period-1 and period-2. (b), (g) and (h) present for period-1, period-2 and period-4. ($E = 69\text{GMa}$, $\rho = 2712\text{kg/m}^3$, $A = 0.0002\text{m}^2$, $J = 2.5\times10^{-9} m^4$, $L = 1.5\text{m}$).

CHAPTER IV

COMPARISION OF NUMERICAL AND ANALYTICAL SOLUTIONS

In this section, the analytical solutions for period-1, period-2 and period-4 solutions are compared with the numerical integration results. The initial conditions for numerical integration are obtained from the analytical solutions.

In these following comparison figures, 'o' always denotes analytical solutions of period-1 motions no matter the solutions are stable or unstable, ' Δ ' represents analytical solutions of period-2 motions no matter the solutions are stable or unstable. Solid line is the 1st period of numerical simulation and dash dot line is the 1000th period of the numerical simulation.

From Fig.4 (a), we can see that the upper branch, which is a loop, has one lower unstable period-1 solution and the other period-1 solution changing its stability due to Hopf bifurcations. While for the lower branch, it has a period-1 solution varying its stability at Hopf bifurcation points. From Tab.1, we check the Hopf bifurcation points HB_7^1 on the upper branch and HB_2^1 on the lower branch, and it shows that HB_7^1 and HB_2^1 occur at 0.8601 and 0.8640, respectively. Therefore, at $\Omega = 0.87$, one unstable period-1 solution from upper branch and two stable period-1 solutions from both upper and lower branches coexist. The time response and the phase portraits of the two stable period-1 solutions from the lower and upper branches are illustrated in the Fig.14 and Fig.15, respectively.

For the lower branch stable period-1 solution which is showed in Fig.14, its initial conditions ($t_0 = 0.0$, $q_{10} = 3.1265\text{e-}3$, $\dot{q}_{10} = -5.8537\text{e-}2$, $q_{20} = -6.7131\text{e-}6$, $\dot{q}_2 = -2.8889\text{e-}4$) is evaluated based on the analytical results of Eq. (3.1). Let the Runge-Kutta numerical

integration start from the above initial condition, the numerical solution and the analytical solution are compared in Figs.14 (a) - (c).

In the time response plot Fig.14 (a), the first several periods and several periods after 1000th periods are presented. Solid lines and circles denote numerical simulation and analytical solutions, respectively.

In the phase portrait Fig.14 (b) & (c), only the 1st period and the 1000th period are given, the 1st period's numerical simulation is plotted by solid curves and the 1000th period numerical simulation is presented by dash dot lines.

From the figures we can see that the 1000th period numerical trajectory is on top of the first period, which means this solution is stable. The match of the circles with solid and dash dot lines means that the analytical solution is accurate.

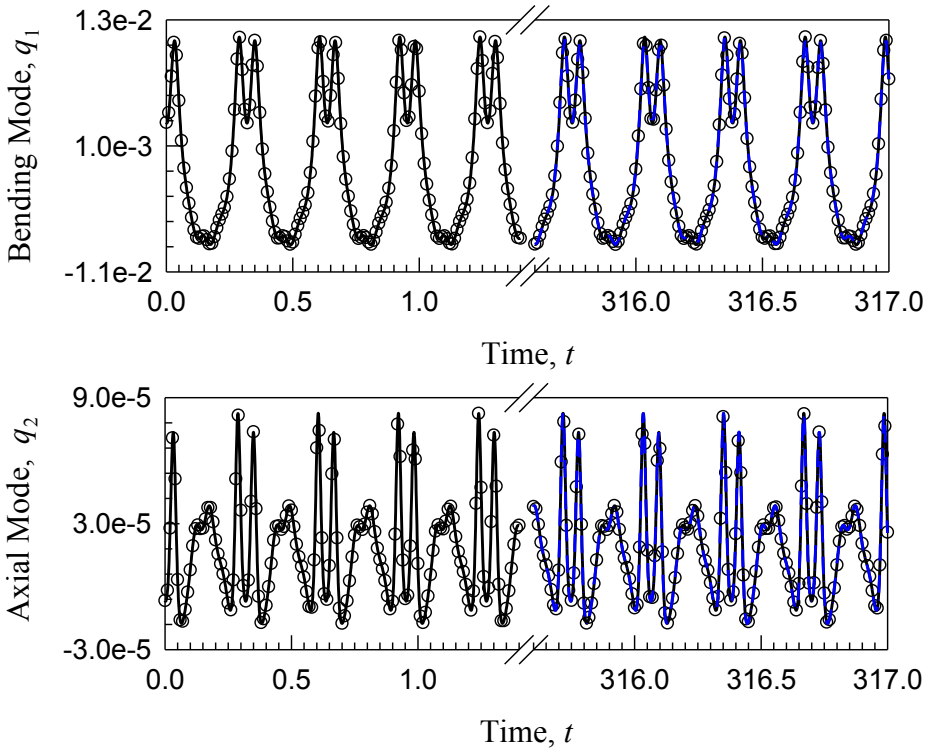

(a)

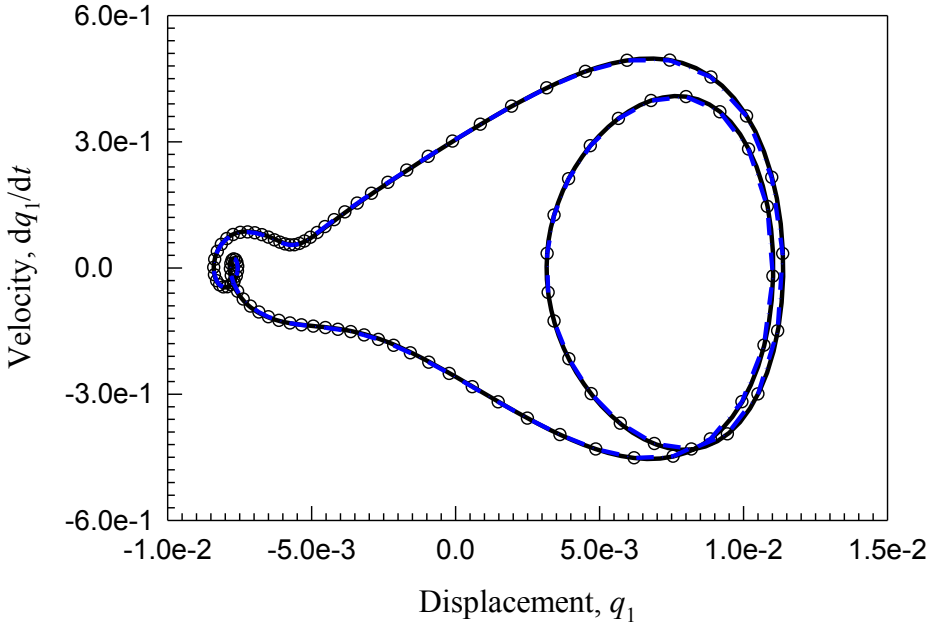

(b)

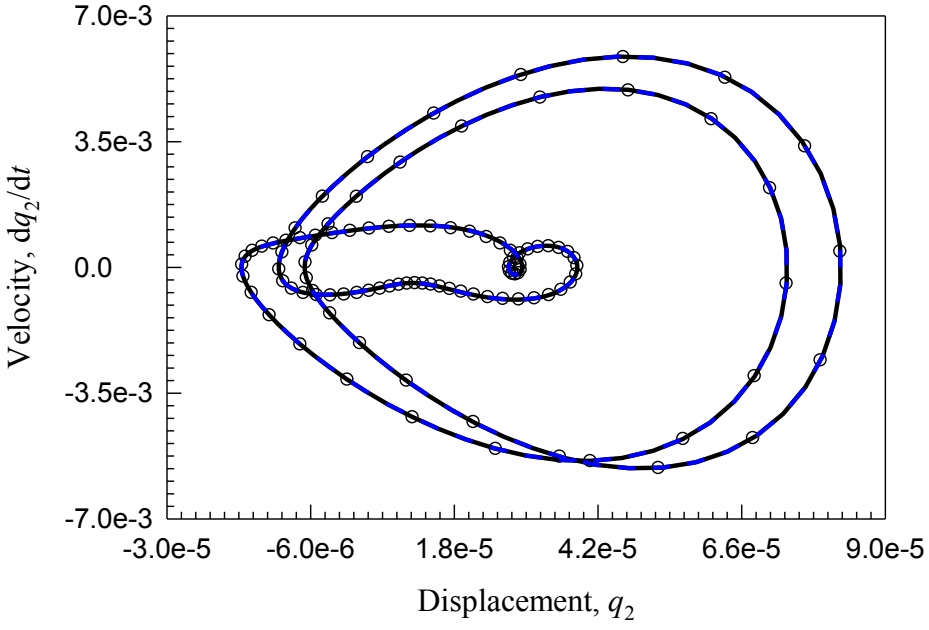

(c)

Fig.14 Comparison of analytical and numerical solutions of the stable period-1 motion from upper branch: (at $\Omega = 0.87$, initial condition: $t_0 = 0.0$, $q_{10} = 3.1265\text{e-}3$, $\dot{q}_{10} = -5.8537\text{e-}2$, $q_{20} = -6.7131\text{e-}6$, $\dot{q}_{20} = -2.8889\text{e-}4$). 'o' denotes analytical period-1 solutions; solid line is the 1st period of numerical simulations; dash dot line represents the 1000th period of numerical simulations.

Similarly, the upper branch period-1 solution at $\Omega = 0.87$ is also stable and its initial condition is ($t_0 = 0.0$, $q_{10} = 7.8719\text{e-}3$, $\dot{q}_{10} = 4.8947\text{e-}2$, $q_{20} = 3.1443\text{e-}5$, $\dot{q}_{20} = 5.1334\text{e-}4$). Fig.15 (a) - (c) illustrate the comparison between the numerical and the analytical solutions.

In the time response plot Fig.15 (a), the first several periods and several periods after 1000th periods are presented. Solid lines denote numerical simulation and circles denote analytical solutions.

In the phase portrait Fig.15 (b) & (c), only the 1st period and the 1000th period are given, the 1st period's numerical simulation is plotted by solid curves and the 1000th period numerical simulation is presented by dash dot lines. The 1000th period numerical trajectory is on top of the first period, which means this solution is stable. The match of the circles with solid and dash dot lines means that the analytical solution is accurate.

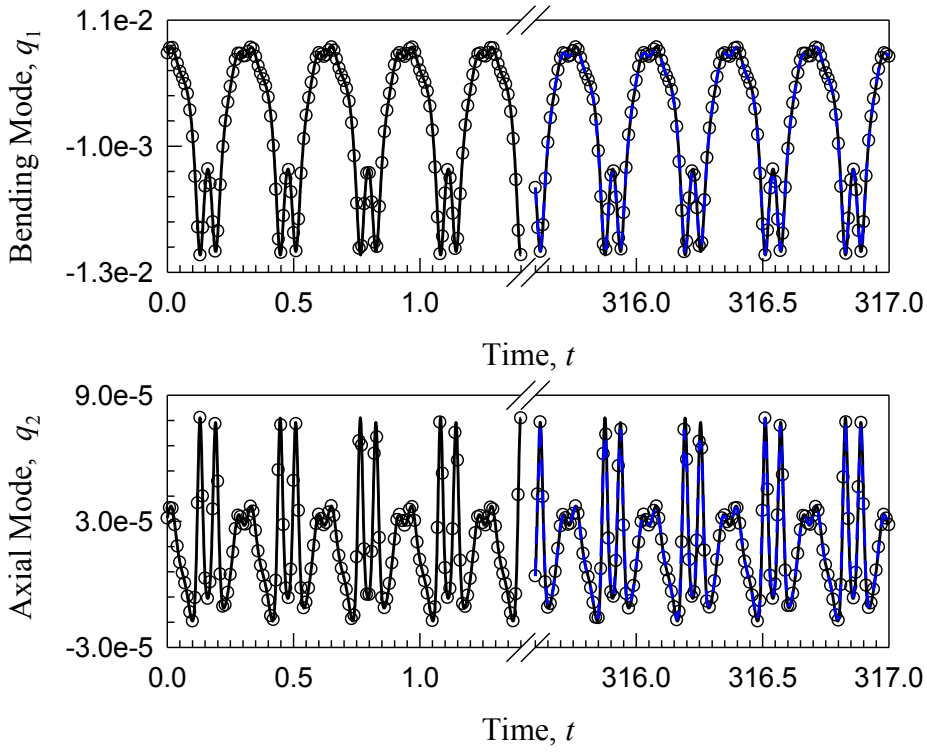

(a)

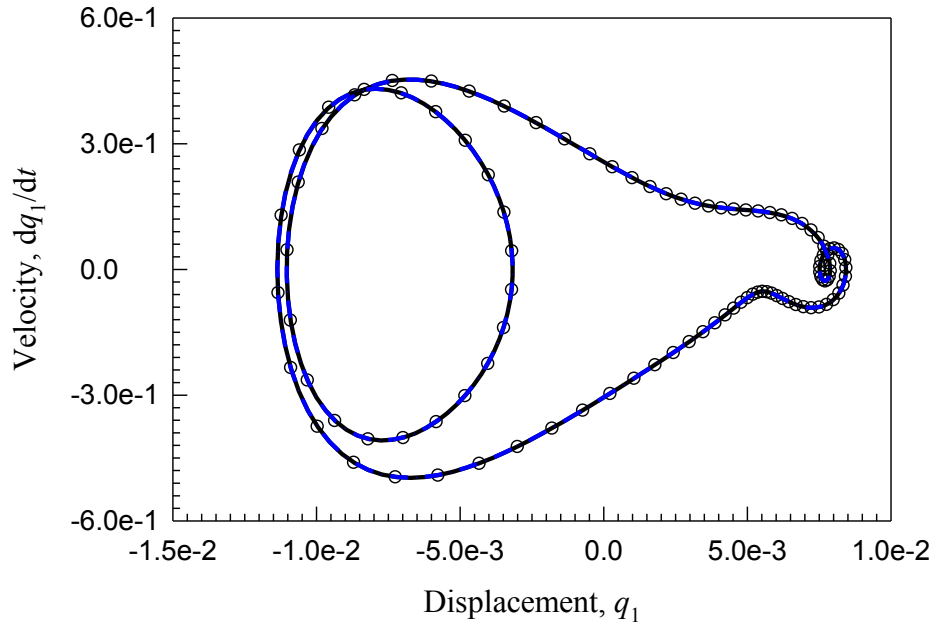

(b)

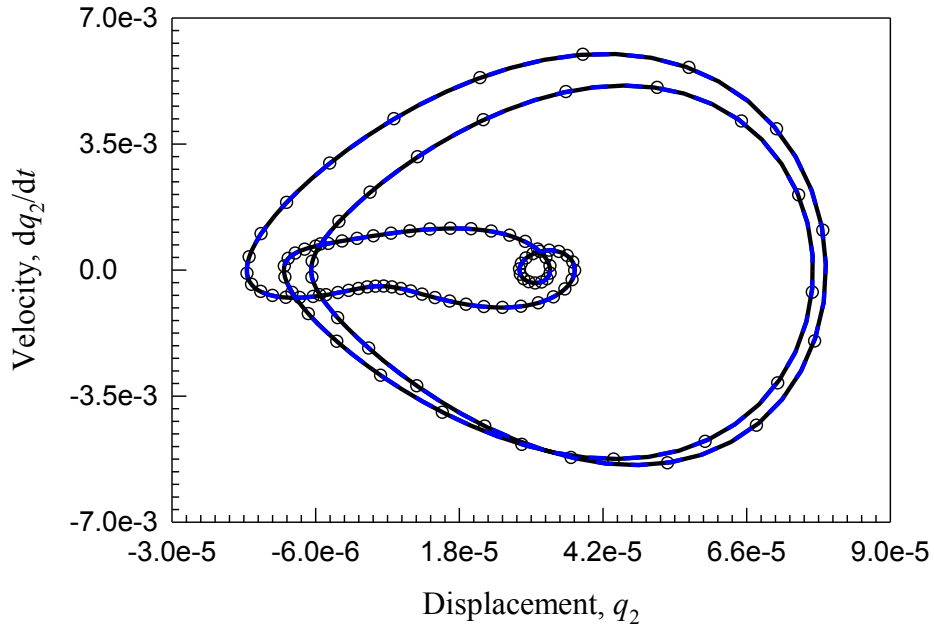

(c)

Fig.15 Comparison of analytical and numerical solutions of the stable period-1 motion from lower branch (at $\Omega = 0.87$, initial condition: $t_0 = 0.0$, $q_{10} = 7.8719\text{e-}3$, $\dot{q}_{10} = 4.8947\text{e-}2$, $q_{20} = 3.1443\text{e-}5$, $\dot{q}_{20} = 5.1334\text{e-}4$). 'o' denotes analytical period-1 solutions; solid line is the 1st period of numerical simulations; dash dot line represents the 1000th period of numerical simulations.

Fig.16 (a) - (c) are the time response and the phase portrait of the unstable period-1 motion on the upper branch at $\Omega = 0.87$, The initial condition of this unstable periodic solution ($t_0 = 0.0$, $q_{10} = 5.0526\text{e-}3$, $\dot{q}_{10} = -1.4767\text{e-}2$, $q_{20} = 4.5280\text{e-}6$, $\dot{q}_{20} = -1.3257\text{e-}4$) is evaluated by Eq.(2.22).

In the time response plot, the first several periods and several periods after 1000th periods are presented. Solid lines denote numerical simulation and circles denote analytical solutions. In phase portrait plot, solid lines and dash dot lines represent 1st period of numerical simulation, 1000th period of numerical simulation. Circles are analytical solutions.

As we can see during the first period on Fig.16 (b) & (c), the numerical simulation is on top of the unstable analytical period-1 solution, and as time progresses the numerical solution moves away from the unstable period-1 solution.

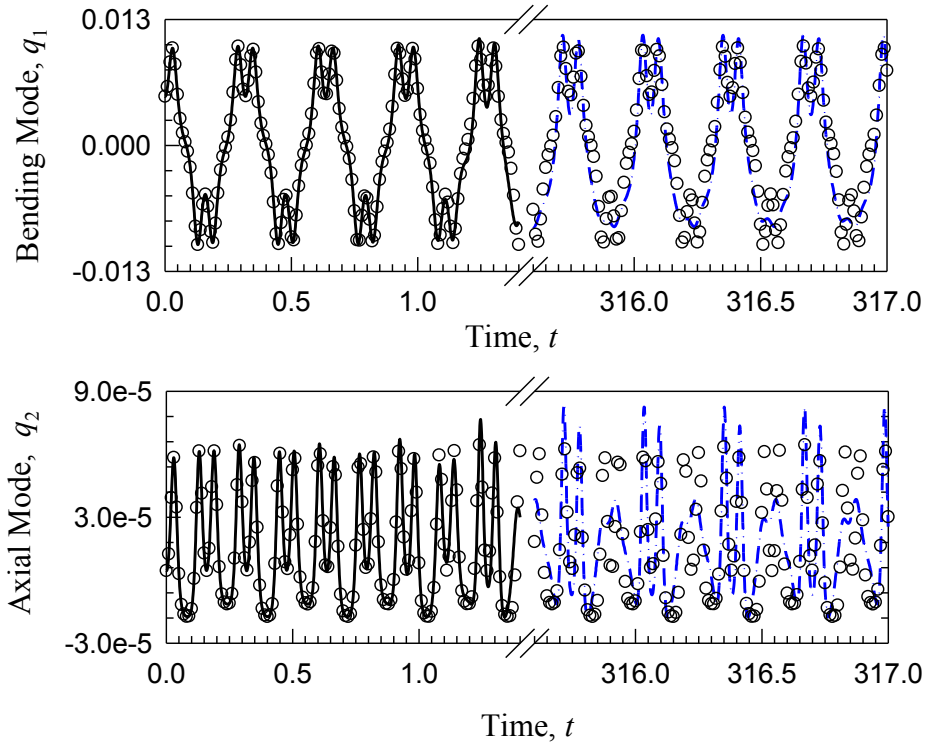

(a)

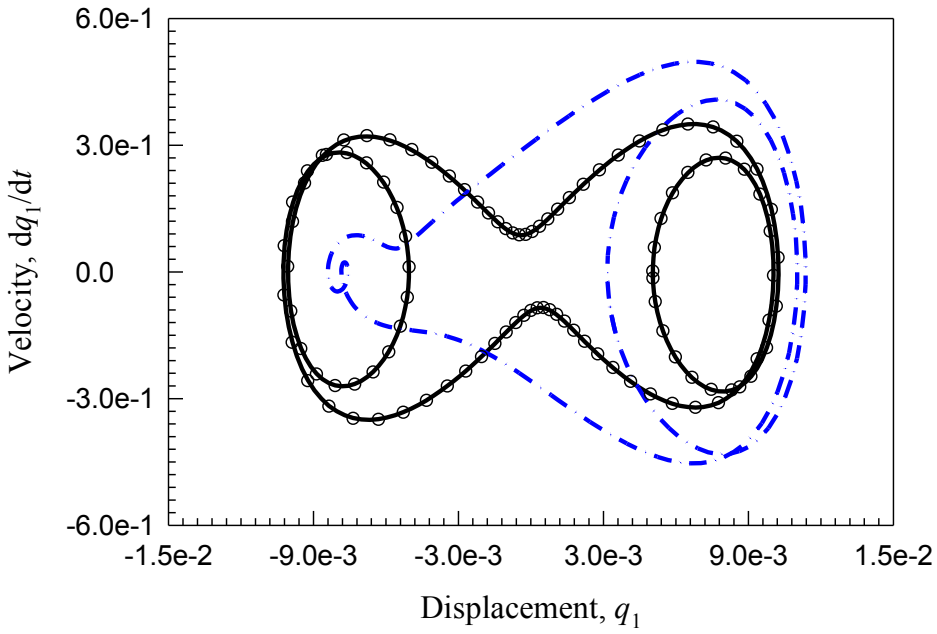

(b)

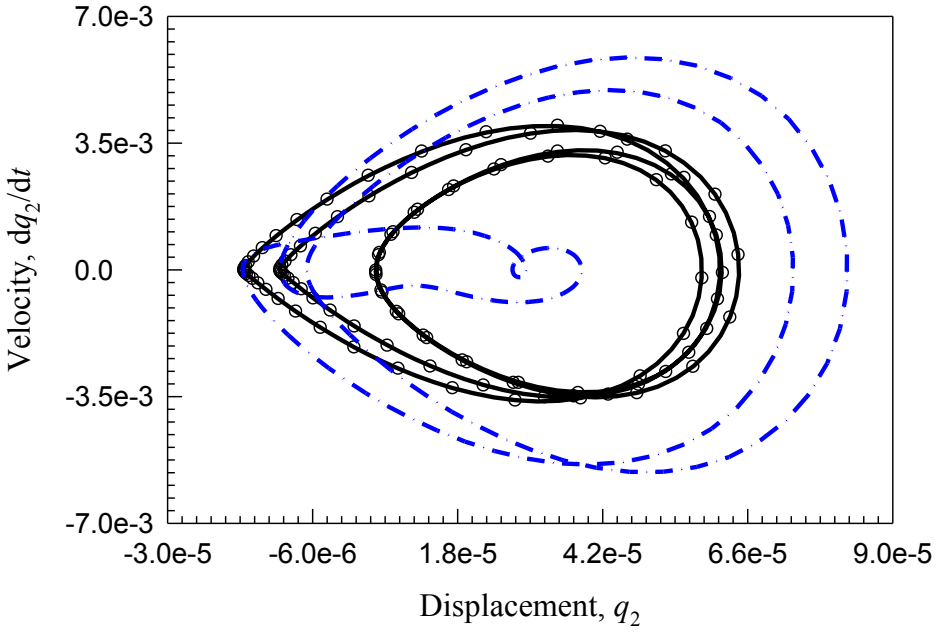

(c)

Fig.16 Comparison of analytical and numerical solutions of the unstable period-1 motion from upper branch: (at $\Omega = 0.87$, initial condition: $t_0 = 0.0$, $q_{10} = 5.0526\text{e-}3$, $\dot{q}_{10} = -1.4767\text{e-}2$, $q_{20} = 4.5279\text{e-}6$, $\dot{q}_{20} = -1.3257\text{e-}4$). 'o' denotes analytical period-1 solutions; solid line is the 1st period of numerical simulations; dash dot line represents the 1000th period of numerical simulations.

From the Fig.16 (b) & (c) and Fig.10 (b) & (c), we can find the 1000th period of the numerical simulation is the same as the lower branch's stable analytical solution. This shows that with initial conditions starting from the unstable period-1 solution of the upper branch, the numerical simulation will converge to the lower branch's stable period-1 solution. The match of the 1st period's numerical results with the unstable period-1 analytical prediction verifies the accuracy of our analytical solution.

Fig.17 (a) - (c) illustrate the time response and phase portraits of another unstable period-1 motion of the upper branch at $\Omega = 0.9757$. Its initial condition is given as $t_0 = 0.0$, $q_{10} = 5.6351\text{e-}3$, $\dot{q}_{10} = -1.7023\text{e-}2$, $q_{20} = 9.1091\text{e-}6$, $\dot{q}_{20} = -1.6987\text{e-}4$. Similarly, solid lines, dash dot lines, and circles represent numerical simulation's 1st period, 1000th period, and the analytical solution.

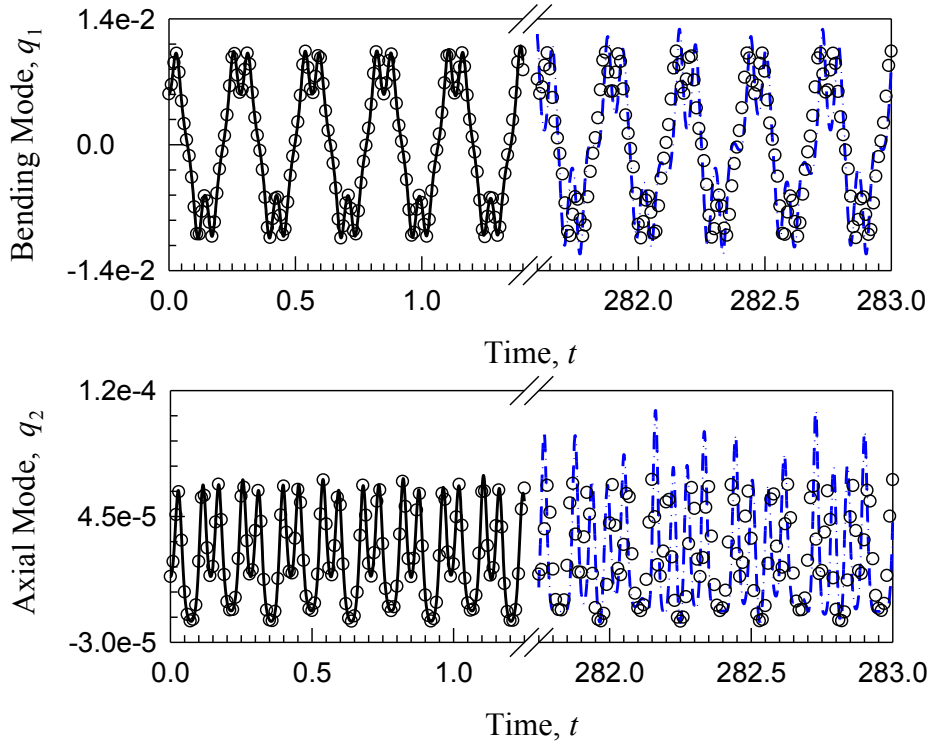

(a)

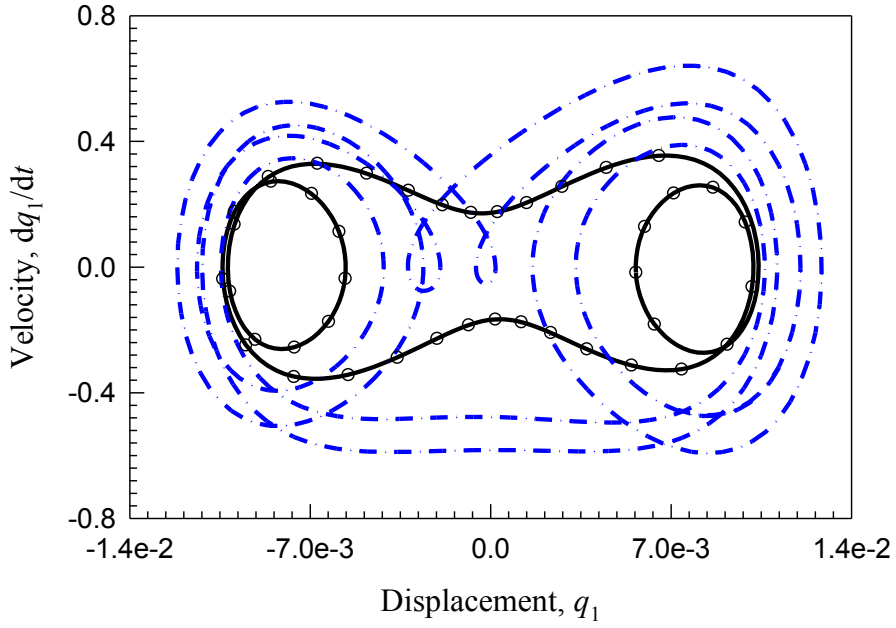

(b)

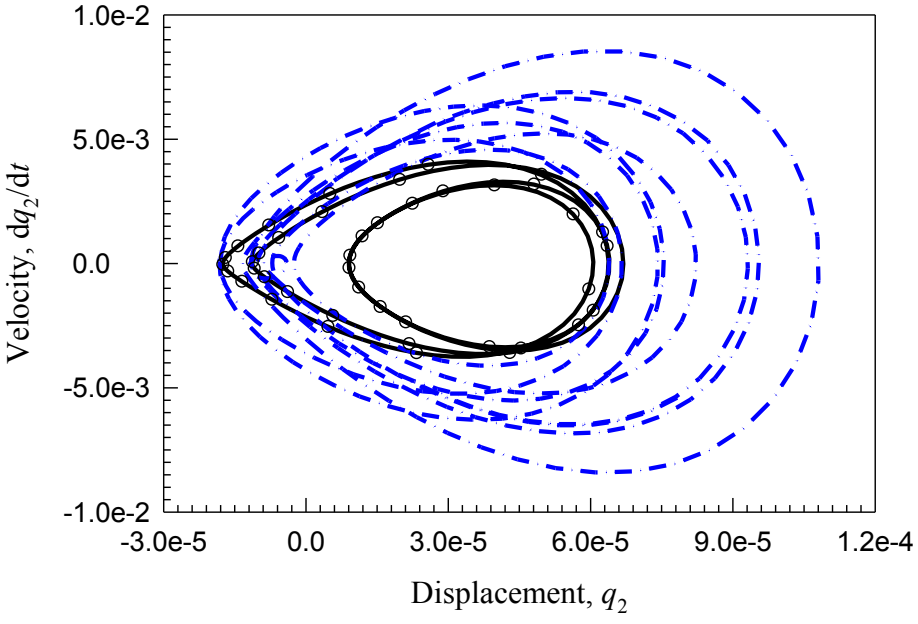

(c)

Fig.17 Comparison of analytical and numerical solutions of the unstable period-1 motion from upper branch: (at $\Omega = 0.9757$, initial condition: $t_0 = 0.0$, $q_{10} = 5.6351\text{e-}3$, $\dot{q}_{10} = -1.7023\text{e-}2$, $q_2 = 9.1091\text{e-}6$, $\dot{q}_2 = -1.6987\text{e-}4$). 'o' denotes analytical period-1 solutions; solid line is the 1st period of numerical simulations; dash dot line represents the 1000th period of numerical simulation.

During the first few periods, the numerical simulation is on top of the unstable analytical period-1 solution, as time progresses the numerical solution finally moves away from the unstable period-1 and converge to a stable period-2 solution on the lower branch.

From Fig.4 (a) and Tab.1, one can find that $\Omega = 0.9757$ is between the occurrence of $HB_3^1 = 0.9453$ and $HB_4^1 = 1.0055$, and in the region $\Omega \in (0.9453, 1.0055)$ the only stable solution on the lower branch is the period-2 solution. We expect the unstable period-1 solution will converge to a stable period-2 solution. The analytical solution and numerical simulation comparison verifies our prediction.

Fig.18 shows the comparison between the numerical solution and the analytical solution of a stable period-2 solution at $\Omega = 0.9537$ on the lower branch. The initial conditions are $t_0 = 0.0$, $q_{10} = 6.3675\text{e-}3$, $\dot{q}_{10} = -5.7921\text{e-}1$, $q_{20} = 1.4803\text{e-}5$, $\dot{q}_{20} = -5.4763\text{e-}3$.

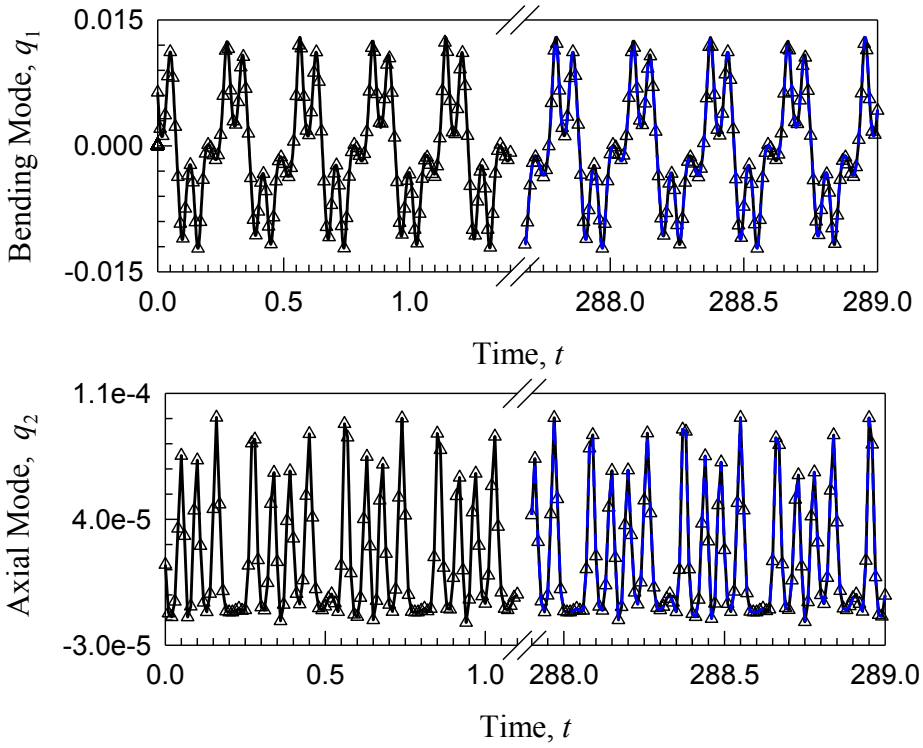

(a)

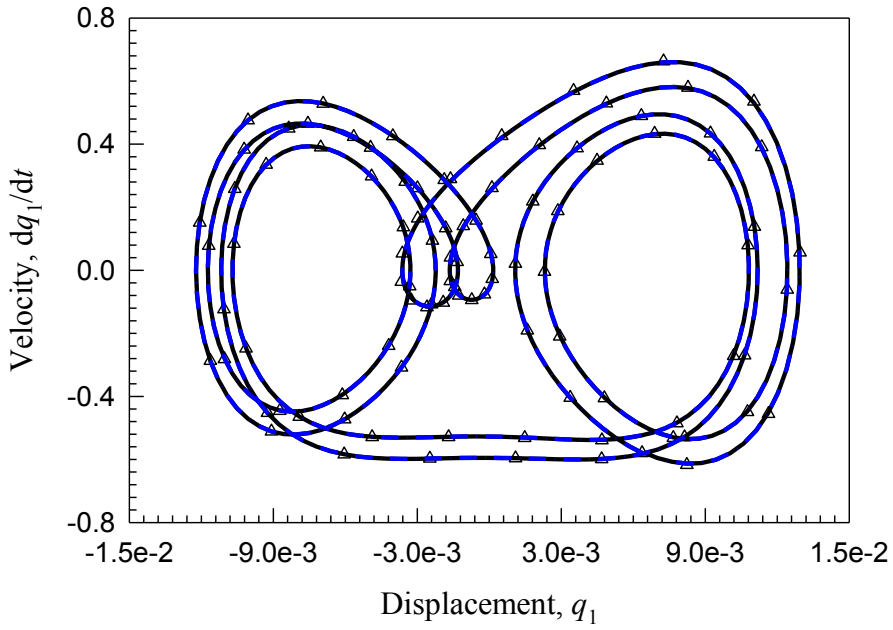

(b)

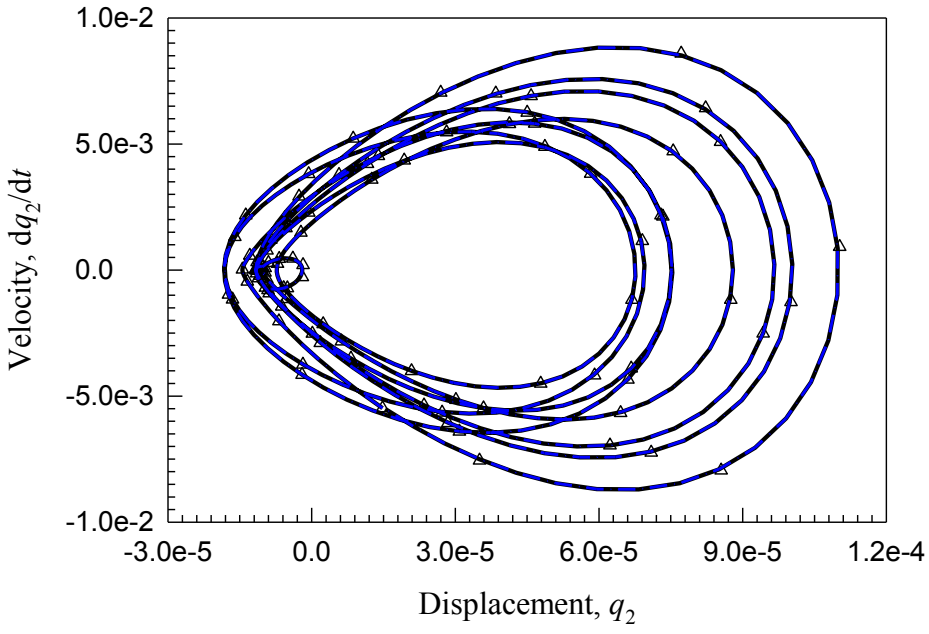

(c)

Fig.18 Comparison of analytical and numerical solutions of the stable period-2 motion: (at $\Omega = 0.9537$, initial condition: $t_0 = 0.0$, $q_{10} = 6.3675\text{e-}3$, $\dot{q}_{10} = -5.7921\text{e-}1$, $q_{20} = 1.4803\text{e-}5$, $\dot{q}_{20} = -5.4763\text{e-}3$). 'Δ' denotes analytical period-2 solutions; solid line is the 1st period of numerical simulations; dash dot line represents the 1000th period of numerical simulations.

In the time response plot Fig.18 (a), the first several periods and several periods after 1000th periods are presented by solid lines and dash dot lines. Triangles denote analytical solutions. In the phase portrait plot Fig.18 (b) & (c), the numerical simulations' 1st period is plotted by solid curves and the 1000th period numerical simulation is presented by dash dot lines, and triangles represent analytical solutions.

From the Fig.18 (a) - (c), we can see that the 1000th period trajectory is on top of the 1st period, which means the solution is stable. Also the triangles analytical solutions match very well with the numerical results.

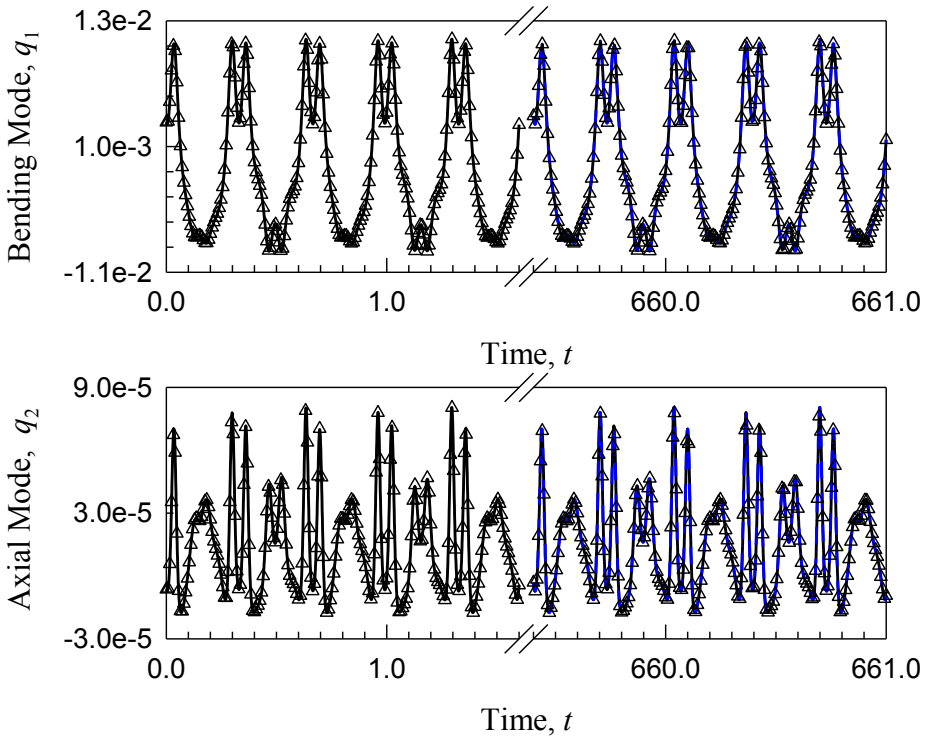

(a)

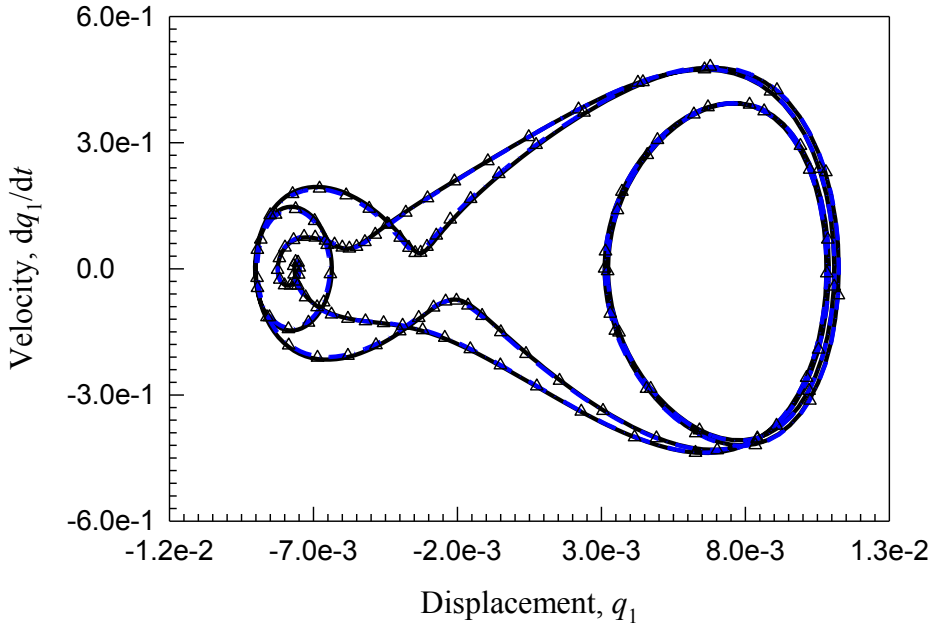

(b)

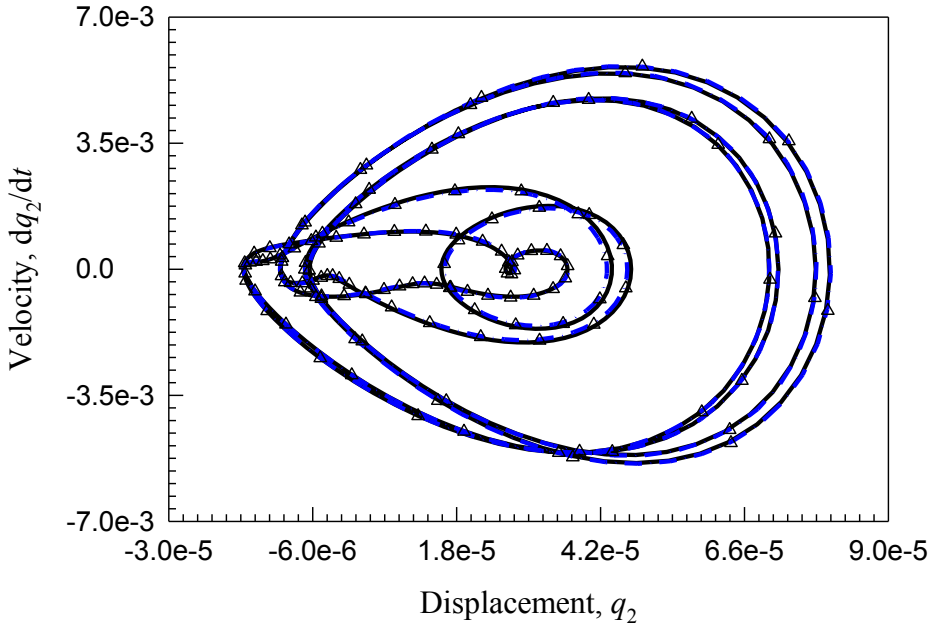

(c)

Fig.19 Comparison of analytical and numerical solutions of the stable period-2 motion (at $\Omega = 0.835$, initial condition: ($t_0 = 0.0$, $q_{10} = 3.3052\text{e-}3$, $\dot{q}_{10} = -1.0629\text{e-}1$, $q_{20} = -6.3562\text{e-}6$, $\dot{q}_{20} = -5.2952\text{e-}4$). 'Δ' denotes analytical period-2 solutions; solid line is the 1st period of numerical simulations; dash dot line represents the 1000th period of numerical simulations.

Fig.19 is the comparison between the numerical solution and the analytical solution of one stable period-2 solutions at $\Omega = 0.835$ on the lower branch. The initial condition are $t_0 = 0.0$, $q_{10} = 3.3052\text{e-}3$, $\dot{q}_{10} = -1.0629\text{e-}1$, $q_{20} = -6.3562\text{e-}6$, $\dot{q}_{20} = -5.2952\text{e-}4$.

In the time response plot Fig.19 (a), the first several periods and several periods after 1000th periods are presented by solid lines and dash dot lines. Triangles denote analytical solutions. In the phase portrait plot Fig.19 (b) & (c), the numerical simulations' 1st period is plotted by solid curves and the 1000th period numerical simulation is presented by dash dot lines, and triangles represent analytical solutions.

From the Fig.19 (a) - (c), we can see that the 1000th period trajectory is on top of the 1st period, which means the solution is stable. Also the triangles analytical solutions match very well with the numerical results.

Figs.20 (a) - (f) are the time response and phase portrait of an unstable period-2 motion. This initial condition which is given by Eq.(2.22) can be written as $t_0 = 0.0$, $q_{10} = 4.1530\text{e-}3$, $\dot{q}_{10} = 6.8194\text{e-}3$, $q_{20} = \text{-}1.5390\text{e-}6$, $\dot{q}_{20} = 2.6450\text{e-}5$.

The comparison of the first several periods' numerical simulation and the analytical solution is illustrated in Fig.16. (a) -(c) and they match very well. Triangles and solid lines represent analytical solution and the 1st period of numerical simulation, respectively.

As integration time progresses, the numerical solution drifts away from the unstable period-2 solution and finally converges to a stable period-4 solution as showed in Fig.20 (d) - (f). The dash dot lines in Fig.20 (d) - (f) are the 1000th period of the numerical simulation, which are also the time response and phase portrait of the stable period-4 motion.

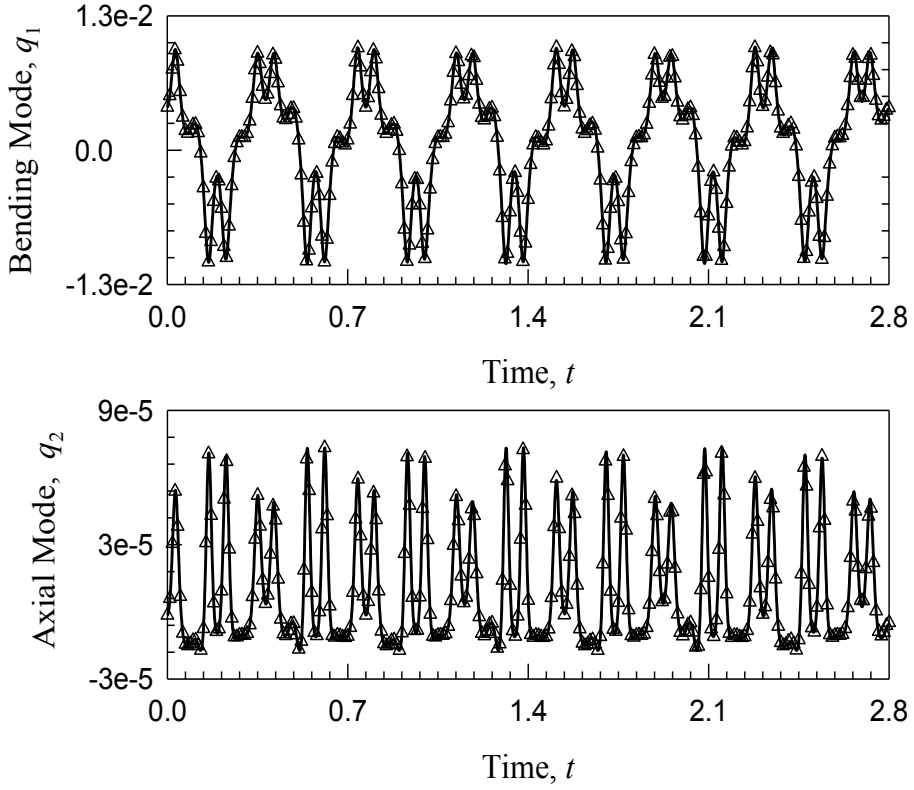

(a)

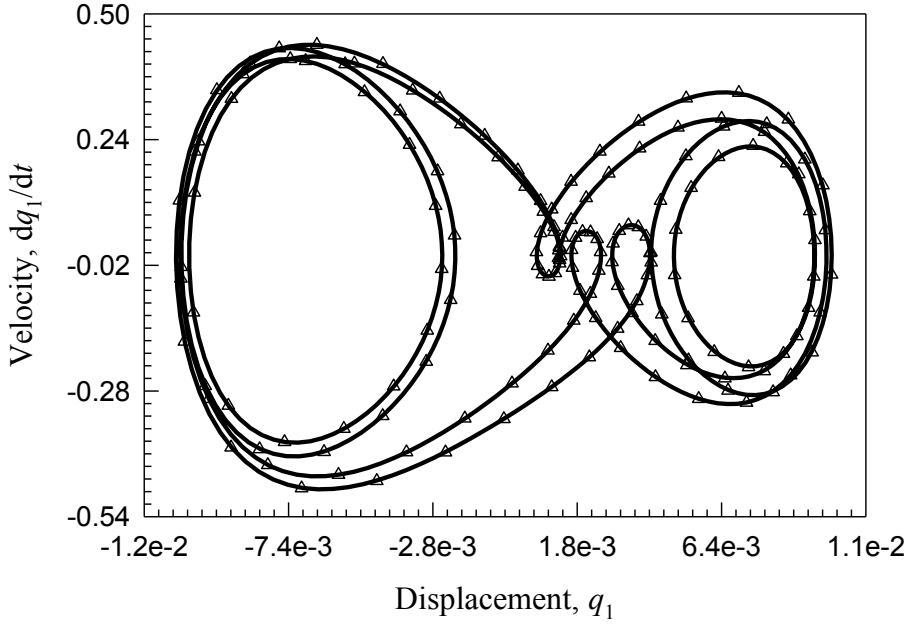

(b)

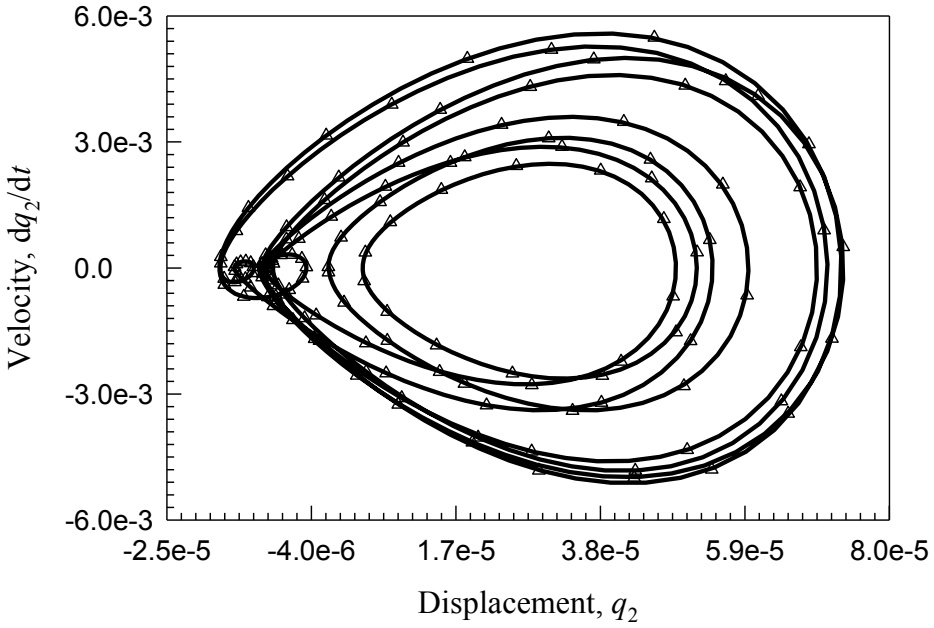

(c)

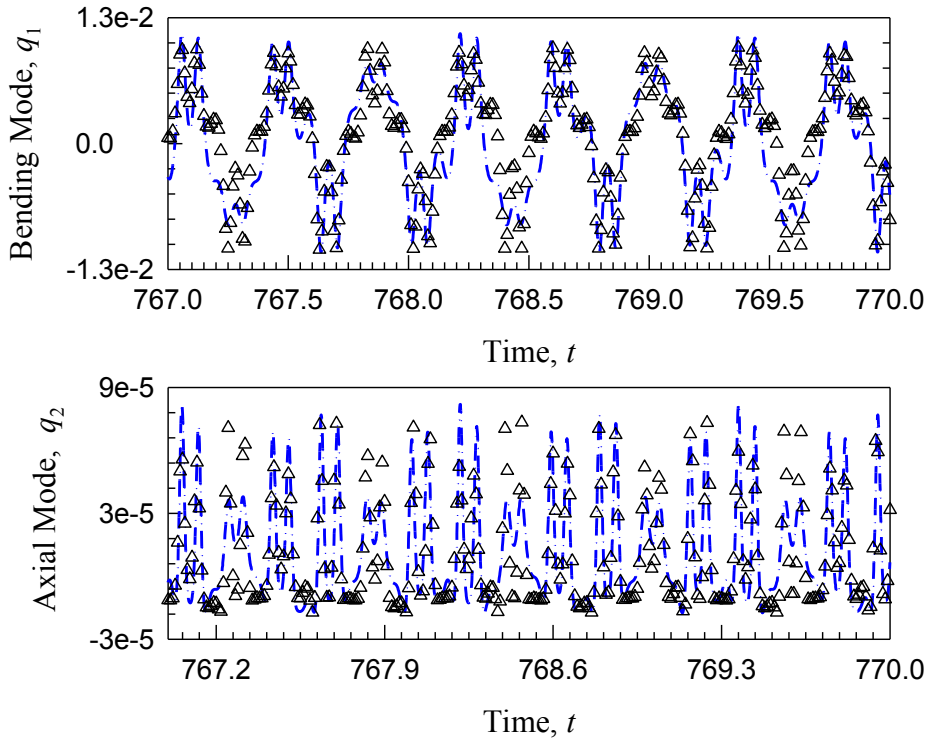

(d)

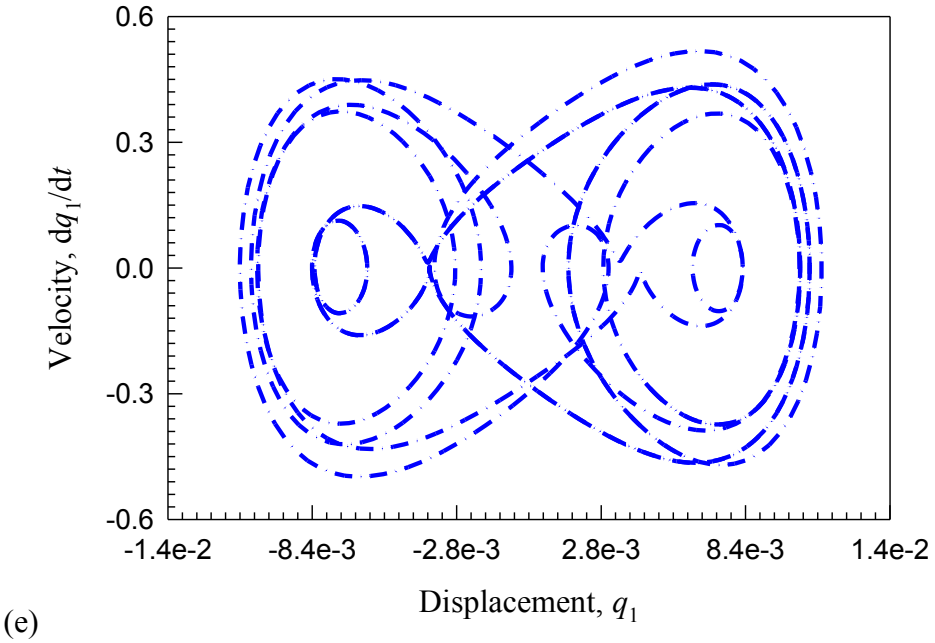

(e)

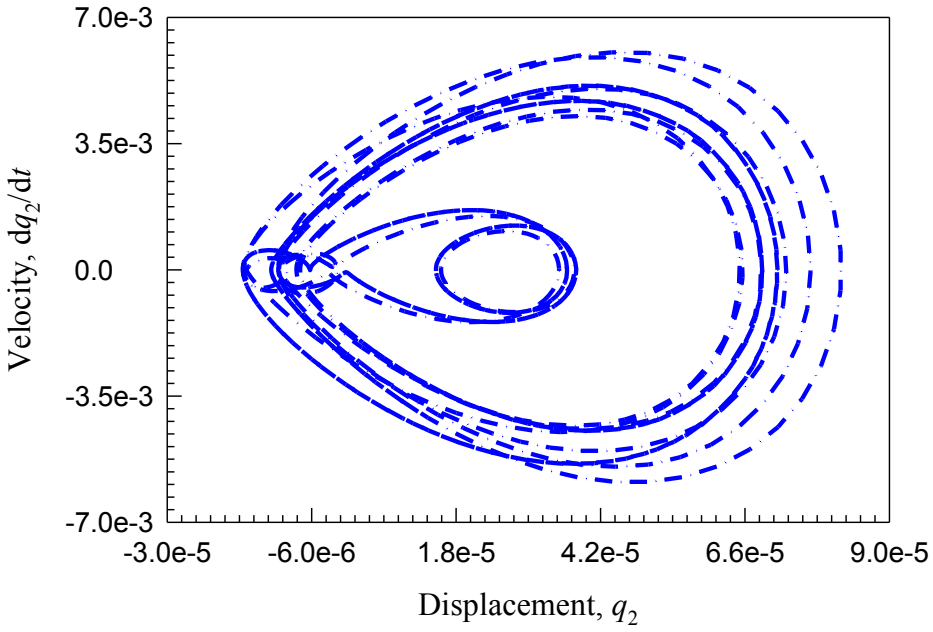

(f)

Fig.20 Comparison of analytical and numerical solutions of the unstable period-2 motion: (at $\Omega = 0.7164$, the initial condition: $t_0 = 0.0$, $q_{10} = 4.1530\text{e-}3$, $\dot{q}_{10} = 6.8194\text{e-}3$, $q_{20} = -1.5390\text{e-}6$, $\dot{q}_{20} = 2.6450\text{e-}5$). '$\Delta$' denotes unstable period-2 analytical solutions; solid line is the 1st period of numerical simulations; dash dot line represents the 1000th period of numerical simulations.

CHAPTER V

CONCLUSION

In this work, all the period-1, period-2 and period-4 motions of a rotating beam with variation rotating speed are studied at the principle resonance region.

A two degree of freedom dynamic model of the rotating beam is obtained by the Galerkin method, in which the strong nonlinear geometric stiffening terms are retained. The amplitude versus frequency bifurcation diagram is presented.

The saddle node bifurcations and Hopf bifurcations of the periodic motions are obtained by the combined implementation of the high order harmonic balance method, Floquet theory, and the Discrete Fourier Transform.

First, a periodic solution is obtained by the high order harmonic balance method, and then its stability and the occurrence of bifurcations with the bifurcation category are determined by the Floquet multiplier. As the excitation frequency increases, numerical continuation method is employed to calculate the next periodic solution represented by the Fourier series. At the Hopf bifurcation point of a periodic solution, the initial predictor of the new generated periodic doubling motion is obtained by the discrete Fourier transform.

The periodic solutions and their bifurcations obtained via the above described approach are verified by numerically integrating the original dynamic system. The Runge-Kutta algorithm is used in the numerical integration, and the initial conditions of all numerical integrations are predicted by the analytical harmonic balance approximation. The comparisons between analytical solutions and numerical integration results show exact match.

In the future, with more than one system parameters varying, the period-2 and period-4 solutions' parametric boundary will be calculated based on our method. These analysis results will help people to better understand the blade bending vibrations and the effects of the vibration on the structure failure factors.

REFERENCES

Schilhansil M.J., 1958, "Bending frequency of a rotating cantilever beam", *Journal of Applied Mechanics,* v 25, 28 - 30.

Hurty W.C. and Rubinstein M.F., 1964, *Dynamics of Structures*. Englewood Cliffs, N.J.: Prentice Hall.

Anderson G.L., 1975, "On the extensional and flexural vibrations of rotating bars", *International Journal of Nonlinear Mechanics,* v 10, 223-236.

Kane T.R., Ryan R.R., and Banerjee, A.K., 1987, "Dynamics of cantilever beam attached to a moving base", *AIAA. Journal of Guidance Control and Dynamics*, v 10(2), 139-151.

Simo J.C. and Vu-Quoc L., 1987, "The role of non-linear theories in transient dynamics analysis of flexible structures", *Journal of Sound and Vibration*, v 119(3), 487-508.

Sharf I., 1995, "Simulation of Flexible-Link Manipulators with Inertial and Geometric Non-linearities", *ASME Journal of Dynamic Systems, Measurement, and Control*, v 117, 74-87.

Sharf I., 1996, "Geometrically non-linear beam element for dynamics simulation of multibody systems", *International journal for Numerical Methods in Engineering*, v 39, 763-786.

Sharf I., 1999, "Non-linear Strain Measures, Shape Functions and Beam Elements for Dynamics of Flexible Beams", *Multibody System Dynamics,* v 3, 189-205.

Bhat R.B., "Transverse vibrations of a rotating beam with tip mass as predicted by using beam characteristic orthogonal polynomials in the Rayleigh–Ritz method", *Journal of Sound and Vibration,* v 105(2), 199 - 210.

Yoo H.H. and Shin S.H., 1998, "Vibration analysis of rotating cantilever beams", *Journal of Sound and Vibration,* v 212(5), 807 - 828.

Hsiao K.M., Yang R.T., and Lee A.C., 1994, "A consistent finite element formulation for non-linear dynamic analysis of planar beam", *Int. j. numer. method eng.*, v 37, 75-89.

Hashemi S.M., Richard M.J., and Dhatt G., 1999, "A new dynamic finite element (DFE) formulation for lateral free vibrations of Euler–Bernouilli spinning beams using trigonometric shape functions", *Journal of Sound and Vibration,* v 220(4), 601 - 624.

Turhan Ö. and Bulut G., 2005, 'Dynamic stability of rotating blades eccentrically clapped to a shaft with fluctuating speed", *Journal of sound and vibration*, v 280, 945 - 964.

Al-Nassar Y.N., Al-Bedoor B.O., 2003, "On the vibration of a rotating blade on a torsionally flexible shaft", *Journal of sound and vibration*, v 259(5), 1237-1242.

Rao J.S. and Carnegie W., 1970, **"**Nonlinear Vibrations of Rotating Cantilever Beam**",** *Aeronautical Journal*, v 74(710), 161-165.

Kosmatka J.B. and Friedmann P.P., 1989, **"**Vibration analysis of composite turbopropellers using a nonlinear beam-type finite-element approach**",** *AIAA Journal*, v 27(11), 1606-1614.

Turhan Ö. and Bulut G., 2008, "On nonlinear vibrations of a rotating beam", *Journal of Sound and Vibration*, v 322(1-2), 314-335.

Yao M.H., Chen Y.P., Zhang W., 2012, "Nonlinear vibrations of blade with varying rotating speed", *Nonlinear Dynamics*, v 68(4), 487-504.

Khaden S.E., Shahgholi M., and Hosseini S.A.A., 2011, "Two mode combination resonances of an in-extensional rotating shaft with large amplitude", *Nonlinear Dynamics*, v 65, 217-233.

Wang F., and Luo A., 2012, "On the Stability of a Rotating Blade with Geometric Non-linearity", *Journal of Applied Nonlinear Dynamics*, v 1(3) 263 - 286.

Wang, F., Luo, A., 2013, "Analytical periodic motions in a parametrically excited, nonlinear rotating blade", *The European Physical Journal Special Topics*, Volume 222, 1707-1731.

Luo, A.C.J. (2012), *Continuous Dynamical Systems*, *HEP-L&H Scientific*, Glen Carbon.

Dentsoras A.J. and Kouvaritakis E.P., 1995, "Effects of Vibration Frequency on Fatigue Crack Propagation of a Polymer at Resonance", *Engineering Fracture Mechanics,* v 50(4), 467-473.

Mees Al. and Rapp P. E. 1978, "Periodic metabolic systems," *J. Math. Biology*, v 5, 99-1l4.

Ruelle D. and Takens R., 1971, "On the nature of turbulence," *communication in mathematical physics*, v 20, 167-192.

Ruelle D. and Takens R., 1971, "Note concerning our paper: `On the nature of turbulence' ", *communication in mathematical physics*, v 23(4), 343-344.

Mees A. and Chua L.O., 1979, "The Hopf Bifurcation Theorem and Its Applications to Nonlinear Oscillations in Circuits and Systems", *IEEE Transactions on Circuits and Systems*, v 26(4), 235-254.

Itovich G.R. and Moiola J.L., "Double Hopf Bifurcation Analysis Using Frequency Domain Methods", *Nonlinear Dynamics*, v 39, 235-258.

Nayfeh A.H. and Mook D.T., 1979, *Nonlinear Oscillations*, Wiley, New York, 1979.

Moiola J. and Chen G.R., 1993, "Computations of Limit Cycles Via Higher Order Harmonic Balance Approximation", *IEEE Transactions on Automatic Control*, v 38(5), 782-790.

Mickens R.E., 1996, *Oscillations in Planar Dynamic Systems*, World Scientific, Singapore.

Jing Z.J., Wang J.L. and Chen L.N., 2002, "Computation of Limit Cycle via Higher Order Harmonic Balance Approximation and its Application to a 3-Bus Power System", *IEEE Transactions on Circuits and Systems —I: Fundamental Theory and Applications*, v 49(9), 1360-1370.

Ajjarapu V. and Lee B., 1992, "Bifurcation theory and its application to nonlinear dynamical phenomena in an electrical power system", *Transactions on Power Systems*, v 7(1), 424-431.

Tamura, H., Tsuda, Y., and Sueoka, A., 1981, "Higher approximation of steady oscillations in nonlinear systems with single degree of freedom," *Bulletin of the JSME*, VOl.23, No. 195, 1616-1624.

Lau, S.L. and Cheung, Y.K., 1981, "Amplitude Incremental Principle for Nonlinear Vibration of Elastic Systems," *ASME Journal of Applied Mechanics*, Vol. 48, 959 - 964.

Lau, S.L., Cheung, Y.K., and Wu, S.Y., 1982, "A variable parameter incrementation method for dynamic instability of linear and nonlinear systems," ASME Journal of Applied Mechanics, Vol. 49, 849-853.

Lau, S.L., Cheung, Y.K., and Wu, S.Y., 1983, "Incremental Harmonic Balance method with multiple time scales for aperiodic vibration of nonlinear systems," ASME Journal of Applied Mechanics, Vol. 50, 871 - 876.

Cameron, T. M. and Griffin, J. H., 1989, "An alternating frequency/time domain method for calculating the steady-state response of nonlinear dynamic systems," ASME Journal of Applied Mechanics, Vol. 56, 149 - 153.

Allgower, Eugene L. and Georg Kurt, 1990, Introduction of Numerical Continuation Methods, Colorado State University.